INCREASING THE RELIABILITY OF FULL-FIELD DIC STRAIN MEASUREMENT BY ADAPTIVE ALGORITHMS

by

Necdet Ali Özdür

B.S., Mechanical Engineering, Boğaziçi University, 2016

Submitted to the Institute for Graduate Studies in
Science and Engineering in partial fulfillment of
the requirements for the degree of
Master of Science

Graduate Program in Mechanical Engineering
Boğaziçi University

2019

ACKNOWLEDGEMENTS

First and foremost, I am deeply grateful to Gizem Kalgıdım for her unconditional love and limitless support that helped me endure hardships I encountered throughout this work. I find the motivation, and will I need in her companionship, to do more and accomplish more.

I am immensely thankful to my parents for raising me as the person I am now. I cannot and will never be able to fully repay their everlasting efforts and sacrifices they pour into my education and well-being. I just hope that I can live up to a son they can be proud of.

I thank to my advisors, Assoc. Prof. C. Can Aydıner for introducing me to new and current topics on materials science and guiding me through a versatile programming language that broadened my horizon and formed the very basis of my thesis, and Assist. Prof. Sertan Alkan for his critical suggestions that highly contributed to the final quality of this work. This work would not be possible without their valuable experience and guidance.

And finally, I would like to thank to my partners in Mechanics of Advanced Materials lab, Enver Kapan, İ. Buğra Üçel, Olcay Türkoğlu, and Nima Shafaghi. Their support and friendship made this otherwise tiring project bearable and fun.

This work was partially supported by B.U. Research Fund at Boğaziçi University under contract 17A06P3.

ABSTRACT

INCREASING THE RELIABILITY OF FULL-FIELD DIC STRAIN MEASUREMENT BY ADAPTIVE ALGORITHMS

Digital Image Correlation is now a widely used method for measuring deformation fields with high spatial resolution. Its single camera (two-dimensional) application is used to evaluate in-plane deformation of a planar surface. A subset based 2D DIC algorithm divides the region of interest of both reference and deformed image into equally spaced subsets and compares them. Matching each subset over the undeformed and deformed images yields the displacement field over the subset grid. Finally, differentiation of the displacement field yields local deformation and rotation parameters. In conventional DIC applications every subset in the grid is evaluated with the same algorithm regarding interpolation and optimization functions. This results in a statistical loss of data points in the DIC grid, in correlation due to factors like weak pattern, poor choice of initial conditions and other operational parameters. This loss might be in the form of matching failure (no data), and wrong evaluations (outlier data). The major aim of this project is to develop adaptive DIC algorithms that can recover the most out of the data and minimize the number of lost data points through recursive analysis. These algorithms will detect outliers and reevaluate faulty points using different initial guesses and parameters until a reasonable measurement is possible at each subset. This more advanced application proposes to recover DIC points that will simply not work with the traditional methods. However, especially in microscopic length scales certain subsets are not physically analyzable regardless of the algorithm, since their DIC pattern is significantly altered or include little to no distinguishable information. This thesis further aims to use a-priori pattern quality measures to detect and factor out weak patterns and pattern alterations in each subset.

ÖZET

TAM SAHA DIC GERİNİM ÖLÇÜMÜ GÜVENİLİRLİĞİNİN UYARLANABİLİR ALGORİTMALAR İLE ARTIRILMASI

Dijital İmge Korelasyonu, deformasyon sahasının yüksek çözünürlüklü uzamsal ölçümü için yaygın kullanılan bir yöntemdir. Bu yöntemin tek kameralı (iki boyutlu) uygulaması düzlemsel bir yüzeyin düzlem içi deformasyon ölçümünde kullanılır. Alt küme bazlı iki boyutlu DIC algoritması hem referans hem de deforme olmuş imge için ilgilenilen alanı eşit aralıklarla alt kümelere böler ve bunları kıyaslar. Her alt kümenin iki imge arasında eşleştirilmesi, alt küme ağı üzerinde yer değiştirme sahasını verir. Son olarak, yer değiştirme alanının türevi, lokal gerinim ve rotasyon değerlerini verir. Geleneksel DIC yazılımları, aradeğerleme ve optimizasyon fonksiyonları açısından ağdaki her alt kümeyi aynı algoritma ile değerlendirildiği için zayıf yüzey deseni, kötü başlangıç koşulları ve diğer operasyonel parametreler gibi faktörlerle bağlantılı olarak DIC ağında istatistiksel veri kaybına neden olur. Bu kayıp, eşleşme hatası (veri kaybı) ve yanlış ölçüm (hatalı veri) şeklinde olabilir. Bu projenin temel amacı, verilerden en fazlasını elde edebilen ve kayıp veri noktası sayısını en aza indirebilen yinelemeli DIC algoritmaları geliştirmektir. Bu algoritmalar, her bir alt kümede makul bir ölçüm mümkün olana kadar farklı parametreleri kullanarak geleneksel yöntemlerle çalışmayacak hatalı noktaları tespit eder ve yeniden analiz eder. Bununla birlikte, özellikle mikroskobik ölçekte bazı alt kümeler, kullanılan algoritmalardan bağımsız olarak, yüzey desenleri önemli ölçüde değiştiğinden veya ayırt edilebilir içeriğe sahip olmadığından analiz edilemez. Bu tez ayrıca, her bir alt kümedeki zayıf yüzey desenlerini ve yüzey deseni değişikliklerini saptamak ve elemek için uyarlamalı algoritma metodolojisini kullanmayı amaçlamaktadır.

TABLE OF CONTENTS

LIST OF FIGURES

LIST OF TABLES

LIST OF SYMBOLS

a_i	Average distance between i^{th} point to remaining points
b_i	Distance from i^{th} point to the nearest cluster centroid
C	Correlation coefficient
d	Grid spacing
D	Pattern degradation
$f,\ g$	Reference and deformed subset
$I,\ J$	Reference and deformed image
M_{sub}	Subset size
p	Probability of occurrence
P	Deformation vector
r	Cross correlation
r_{pb}	Point biserial correlation coefficient
s_i	Silhouette coefficient of i^{th} subset
S	Pattern entropy
$u,\ v$	Displacement in x and y coordinates
$u_x,\ u_y$	Partial derivative of u with respect to x and y
$v_x,\ v_y$	Partial derivative of v with respect to x and y
w	Change in average pixel-level
$\overline{Y}$	Dichotomous variable
z	z-score standardized value
ϵ	Infinitesimal strain
ϵ_{tol}	Tolerance for termination
μ	Mean
$\tilde{\mu}$	Median
ω	Infinitesimal rotation
σ	Standard deviation

LIST OF ACRONYMS/ABBREVIATIONS

2D	Two Dimensional
DFT	Discrete Fourier Transform
DIC	Digital Image Correlation
FEM	Finite Element Method
NMSE	Normalized Mean Squared Error
RANSAC	Random Sample Consensus
SSIM	Structural Similarity
STM	Scanning Tunnel Microscope
XFEM	Extended Finite Element Method

1. INTRODUCTION

1.1. Motivation

Digital Image Correlation (DIC) is a non-interferometric method to find, compare and track the changes between two images of a specimen under inspection. The intensity patterns of each image are represented by discrete functions and assumed to correspond to each other in a one-to-one and unique manner. By measuring these correspondences, deformation field of the object can be generated. The ability to provide full-field displacement and strain maps makes DIC a particularly useful tool and thus, complementing fundamental but rudimentary materials science tests, such as tensile test and the like. For example, surface of a tensile specimen can be photographed before (reference image) and after (deformed image) loading. Then these images are fed to the DIC algorithm, which in turn computes the displacement and strain information.

A setup consisting of a single gray scale camera with adequate resolution and a white light source is sufficient to record the images of a test specimen [1]. Moreover, if the surface of the specimen has an already discernible pattern on it for the software to track, no extra preparation is needed; otherwise, a manual application of speckle pattern that sticks to and deforms with the surface is required to increase the amount of trackable information [2]. Together with the increasing availability of cheaper processing power, DIC analysis has become popular in the community of materials engineers and scientists over the last decade [1].

DIC has no inherent length scale and it has found use even with atomic force microscopy imaging at a nanometer scale. Consequently, microscopic implementation of DIC has emerged as an important materials science field to easily measure local deformation fields and their micro-mechanisms. Especially, the use of optical microscopy in DIC applications enables scanning of large surfaces with statistical significance that paves the way for comprehensive and detailed investigations of material deformation [1]. However, in optical imaging, many error sources are aggravated when

the imaging length scale is pushed towards microscopy. The application of a successful pattern becomes more difficult; the sharpness is limited by the diffraction limit of light microscopy; the dynamic range of the imaging drops; and microstructural variations affect the images [1]. Especially in the latter case, alteration of the actual pattern on the tracked subset becomes a large issue. This is typically a physical alteration and not a measurement error.

In recent years, much work has been done for the DIC method aiming increased accuracy and computational efficiency. However, it is difficult to pinpoint exact causes of measurement errors in a DIC analysis. As a matter of fact, DIC method lacks a concrete theoretical model that predicts the accuracy and precision of measurements. Yet, it is possible to find studies that evaluate how individual parameters of the DIC implementation affect the displacement measurement accuracy [3–9]. The accuracy of the analysis results mainly depends on the quality of the imaging hardware and the intricacies of the selected correlation algorithm [1]. Therefore, one can classify the causes of DIC errors into two main categories as hardware-related and software-related.

Hardware-related errors are associated with loading, specimen, and imaging. First, speckle pattern on the specimen surface has a great impact on the DIC measurement. Parameters like mean speckle size [10], subset entropy [11], sum of square of subset intensity gradients [12], mean intensity gradient [13] and mean subset fluctuations [14] are proposed as early indicators of pattern quality. Non-parallelism between the camera sensor and the specimen surface under 5° is shown to keep the error lower than other sources of errors [15]. Also, if the camera is placed close to the surface, the change in distance between surface and the camera sensor due to the out-of-plane displacements have a greater impact on the result, since the magnification of the surface features will differ. This error can be reduced by placing the camera further from the object or by using a telecentric camera [9]. Another hardware-related error is the distortions in the image due to low-cost imaging systems. There are methods to calibrate the image digitally for different types of cameras [1]. Finally, any type of noise introduced during imaging will proportionally increase the random error. The effect can be reduced using prior filtering and proper correlation criteria [6, 16–18].

The DIC displacement measurement is also affected by the implemented algorithm, and major algorithmic parameters and their effects on the measurement are well-studied in the literature. Selected size for subsets (small sub-regions of the image that are used to track deformation) should be small enough to fit the selected deformation model; but large enough to contain enough trackable information [19]. Deformation model can include first order or even second order derivatives of translations, depending on the severity of deformation [7, 19, 20]. The correlation criteria, which are used to measure the similarity between reference and deformed subsets, are shown to be less prone to errors if they factor into scalar shifting and scaling of intensity [6, 21, 22]. Optimization algorithms that use Newton's method are quadratically convergent and found to be more reliable in terms of sub-pixel image registry; but they are also computationally costly [3, 23, 24]. To reduce this cost, an approximation to the Hessian matrix is suggested [25,26] and an inverse compositional method that does not require repeated calculations of Hessian matrix is proposed [26–29]. To improve the quality of initial guesses for the registration algorithm, a method is devised to follow a reliable analysis path over images [30]. And last but not least, higher order interpolation functions are found to perform better at extracting pixel intensity values at non-integer coordinates [8, 31]. The details of DIC algorithm and its common components will be discussed in the following section.

As detailed in the earlier paragraphs, there are many studies in the literature, conducted to improve the overall quality in different aspects of the DIC method. Yet, conventional DIC algorithms opt for a "one-size-fits-all" approach and use the same parameters throughout the computation, even though subsets in a typical image lack consistency; this is particularly true for microscopic length scales as the heterogeneity of the material surface and deformation becomes more apparent with the increased magnification. In that case, factors like weakly featured or disrupted patterns can irreversibly spoil considerable amount of data. Furthermore, more data can be lost unnecessarily due to poor choice of initial conditions (that carried over prior incorrect calculations), ineffective correlation functions and other operational parameters (that may not be suitable for some regions of the image under inspection). In the latter case, the data can be recovered by a different set of initial guesses and more robust

optimization algorithms.

There are a handful of studies to develop algorithms that adapt the variations in the compositions of images, by adjusting the weights or gray-level distribution of pixels within a subset [32–34], by using irregularly shaped subsets to include sufficient speckle pattern [35], by autonomously detecting discontinuities [36] or by filling in points of failed optimizations using successful optimizations as boundary conditions in a peridynamics analysis [37]. Even so, literature in self-adaptive algorithms in DIC is limited, and there is still available room for improvement. In that sense, predicting error sources beforehand and detecting mistakes in optimizations may be the key to develop a better adaptive algorithm.

1.2. Fundamentals of DIC

subset based DIC is the conventional approach [2]. Displacement is measured from the coordinate difference of matched subsets from reference and deformed images. Subsets are arranged on a uniform subset grid in general to gather equally spaced displacement data. However, evaluation of each subset is independent, thus compatibility of displacement fields is not guaranteed. On the other hand, mesh-based DIC imposes compatibility on neighboring nodes by meshing the area of interest and matching the entirety of the mesh [38]. The displacements of element nodes represent the displacements of pixels. The basis functions that are used to fit the displacements can be selected as spline functions, i.e. the functions used in finite element method (FEM) or the extended finite element method (XFEM). The latter can also allow for discontinuities and singularities such as cracks and excessive strains within an element [39].

In subset based DIC, the deformation within a subset is assumed to be continuous; therefore, neighboring pixels in the reference subset also assumed to stay as neighbors in the deformed subset. This means each pixel at a coordinate (x, y) on the reference subset f is mapped to a unique point at $(\tilde{x}, \tilde{y})$ on the deformed subset g, according to

the mapping (or shape) function [1, 25]. Then, ideally for all points within a subset:

$$f(x, y) = g(\tilde{x}, \tilde{y}) \tag{1.1}$$

and

$$\tilde{x} = x + u(x, y) \tag{1.2a}$$

$$\tilde{y} = y + v(x, y) \tag{1.2b}$$

where $u(x, y)$ and $v(x, y)$ denote the displacements at point (x, y) in x and y directions, respectively.

For a sufficiently small subset, the local mapping function within a subset can be approximated by a Taylor expansion around subset center (x_0, y_0) as follows:

$$\tilde{x} \approx x + u(x_0, y_0) + \frac{\partial u(x_0, y_0)}{\partial x}(x - x_0) + \frac{\partial u(x_0, y_0)}{\partial y}(y - y_0) + \cdots \tag{1.3a}$$

$$\tilde{y} \approx y + v(x_0, y_0) + \frac{\partial v(x_0, y_0)}{\partial x}(x - x_0) + \frac{\partial v(x_0, y_0)}{\partial y}(y - y_0) + \cdots \tag{1.3b}$$

If the reference subset only undergoes a rigid-body translation, a zero-order mapping function will be sufficient. In most DIC applications, a first-order mapping function is chosen, as it allows normal strains, shear, rotation, translation, and their combinations [2]; for more complicated subset deformations, second-order function can also be used [20]. The forms of the first and second order mapping functions are depicted in Figure 1.1 below.

The subset denotes the small image region which is tracked using the signature of the intensity pattern within and it is has a definitive effect on the accuracy and resolution of the subset based DIC algorithms. A relatively large subset contains abundant information that makes it easily distinguishable in between pre- and post-deformation configurations, but it necessitates high-order shape functions and decreases the "resolution" of the displacement measurement [1, 12]. Thus, it can introduce larger

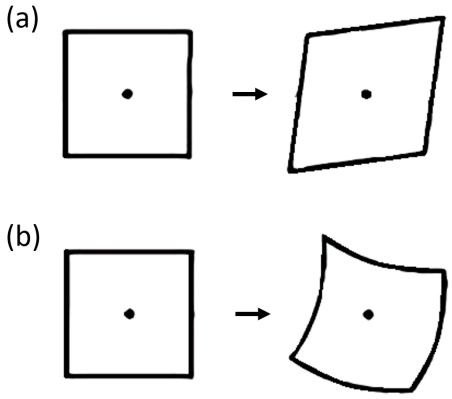

Figure 1.1. Deformation of a subset under (a) first-order, (b) second-order mapping functions.

errors over rapidly changing displacement fields. In contrast, a smaller subset size can easily be approximated by first or second-order shape functions and provides a higher resolution. However, an excessively small subset will not contain sufficient signature to be tracked uniquely and accurately.

Smaller subset sizes with lower order shape functions are mostly preferable due to their reliability in accurate displacement measurement. However, one should evaluate the tradeoff between trackable pattern content and spatial resolution before choosing the right subset size.

The difference between patterns within the reference and deformed subsets is quantified by a correlation coefficient $C(f(x,y), g(\tilde{x},\tilde{y}))$. To calculate its value, the discrete pixel values of patterns should be gathered from reference and deformed images. On the other hand, location and motion of particles on the specimen surface is not confined within the boundaries of pixels located at integer valued coordinates. Therefore, a subpixel interpolation must be applied to convert the discrete image into a continuous surface and find the values that lie on non-integer coordinates within the deformed subset (as shown in Figure 1.2).

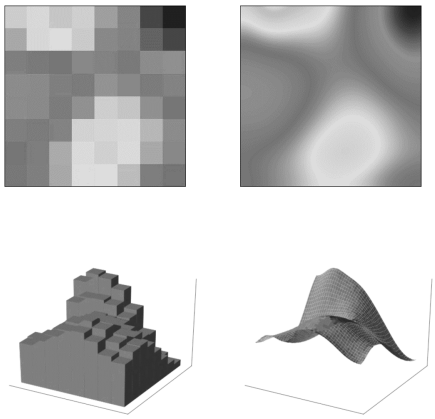

Figure 1.2. Discrete image data (left), spline interpolation of discrete values (right).

The main objective of DIC is to find a mapping vector $P(u, v, u_x, u_y, v_x, v_y)$, that minimizes the difference between reference and deformed subset patterns, therefore minimizing the correlation coefficient at $C(P)$ (0 means perfect correlation, 1 means no correlation). In order to find the global minimum, or a close approximation of it, strictly speaking, an initial guess for the vector P is necessary. If P_0 is the initial guess of the solution P to C, then the solution can be approximated by a second order Taylor expansion:

$$C(P) \approx C(P_0) + \nabla C(P_0)^T (P - P_0) + \frac{1}{2}(P - P_0)^T \nabla\nabla C(P_0)(P - P_0) \tag{1.4}$$

Taking the derivative of Eq. 1.4 and simplifying it while noting that $C(P) = 0$ since P is the solution, the following expression is obtained:

$$P = P_0 - \nabla\nabla C(P_0)^{-1} \nabla C(P_0) \tag{1.5}$$

where $\nabla C(P_0)$ is the Jacobian, $\nabla\nabla C(P_0)$ is the Hessian of C at P_0.

The guess for P is iteratively updated using Eq. 1.5 until a minimum value in C is reached (Figure 1.3). The above optimization method is also called as Newton-Raphson method (or Newton's method), and various forms of it is used in a number of

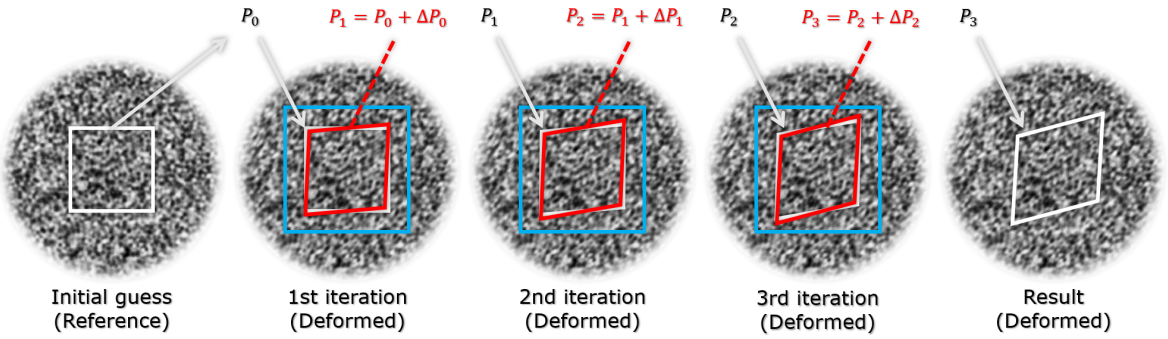

Figure 1.3. Flow of the optimization process. White quadrilaterals denote the current guesses of the deformation, and red quadrilaterals denote new estimates. Areas marked with blue squares denote interpolation zones.

DIC software algorithms, as it shows quadratic convergence near the minimum. That is why the accuracy of the initial guess is highly important, for the iterations to converge and to converge to the correct result, not some other local minimum.

Estimating an initial guess for every point is time-consuming, especially if the deformed subset underwent a heavy deformation. So, calculated deformation vector from a neighboring point is used as an initial guess to cut down on computational time. Usually, a region of interest is defined on the reference image before running the DIC program, and this region is divided into equal, rectangular grids. Computation is done on the equally spaced points within this region. In subset based DIC, computation starts from some point and then continues along a specified path until all points are covered. However, this introduces a path-dependency in the solution procedure. Consequently, a discontinuity in the deformation or an occasional error in optimization at a data point carries over to the following points, leading to incorrect or failed results [2].

1.3. Optimization Failures in DIC

DIC analysis at a data point is said to be failed, when the optimization at that point fails to converge within the given constraints. But occasionally, the algorithm may report a successful optimization, even though it converges to an incorrect result

(i.e. to a local minimum), or the global minimum it converges is heavily altered due to comparatively high levels of noise. Such optimization results can reveal themselves to the naked eye in forms of high-strain dipoles as shown in works of Aydıner and Telemez (2014), or localized clusters that show unusual strain characteristics deviating from the expected strain patterns. Abundance of these false positives particularly clouds the success of remaining data points as they reduce the credibility of the analysis. Therefore, both types of DIC error are considered as faults in this study. Other than hardware related problems, causes of faulty DIC measurements can be grouped in four categories: insufficient pattern information, pattern degradation, high deformation gradients, and poor initial guesses. Among these error sources, first two can lead to irredeemable loss of data in extreme cases; errors caused by other two can be fixed by proper choice of optimization algorithms.

1.3.1. Insufficient pattern information

Simply put, DIC tries to find a unique match to a reference pattern by iteratively changing the shape of a search window that traverses a target image. However, since the information content within an image is not always uniform and/or the selected search window is too small to contain meaningful information, sometimes the pattern that is searched for may have a weak signature, which makes it difficult to find its accurate match. This problem can somewhat be addressed by manually applying a speckle pattern on the photographed surface beforehand to increase the signal strength but maintaining a near-uniform information content throughout the image becomes physically difficult at microscopic length scales. Such imperfect paint speckle applications may lead to areas free of any speckle or obstructed by large paint blotches. Either way, the actual signal received from the image is drowned-out, which makes subsets in these regions virtually untraceable.

1.3.2. Pattern degradation

An eventual side-effect of large deformation is the degradation of surface pattern. The deformation may change the surface reflectivity such that certain regions appear

darker or brighter than before. It may have out-of-plane components that alter surface topography, or the deformation can be so large that material is ripped apart (crack formation) at some places. Such alterations of surface pattern disrupt the one-to-one correspondence of pixels between reference and deformed images, which breaks the underlying assumption of DIC method.

Pattern degradation can also occur if some airborne particulate (i.e. dust) lands on specimen surface in between different load states. Such particles may block substantial pattern information that is present in the reference image, hence causing erroneous results in the DIC analysis within those regions.

1.3.3. High deformation gradients

Materials can undergo abrupt deformations in small regions (due to crack propagation, twin formation, phase transformations etc.) which makes these cases inherently challenging in implementation of DIC in terms of both the satisfaction of the assumptions in the underlying theory as well as the computational limitations. In case, complex deformations with localized high gradients (or even discontinuities) are present in a given subset, the assumed mapping function may not accurately represent the deformation. Similarly, algorithms that rely on passing optimization result of a previous data point to the next are likely to fail at such high-deformation zones since the difference in deformation between two adjacent data points are too high and the provided initial condition stands out to be substantially deviating from the actual result. This problem becomes even more apparent at sparse data grids, where deformation measurement is done in infrequent intervals.

1.3.4. Poor initial guesses

Among the causes of DIC failures, perhaps the hardest one to detect is poor initial guesses because it is hard to visualize and predict it as the number of dimensions of the parameter space is increases. Briefly, closeness of an initial guess to the actual minimum does not guarantee a successful minimization; even though a guess is close

to the result, a roughness in the topography of correlation function may hamper the minimization algorithm from reaching it under given constraints.

1.4. Scope

In this study, strain measurement reliability of digital image correlation, DIC, method at microscopic scales is investigated. As explained in Section 1.3, DIC failures can originate from different sources and indicate themselves in a unique manner; therefore, analysis results and images used in analyses are examined in multiple aspects.

The main purpose of this thesis is to demonstrate that it is possible to automatically redeem and fix erroneous optimizations (which are usually left out by conventional DIC algorithms) as much as possible with recursive passes of DIC that are targeted towards detected faults, thereby reporting credible strain measurements. Moreover, this thesis aims to provide a-priori quality measures on information content and degradation of a pattern that can signalize such errors beforehand. Threshold values for these quality measures that are indicative of whether a data point is irrecoverable or not are also sought.

To this end, this thesis will focus on four test image pairs photographed by a single gray scale optical microscope during automated surface scans of various materials in the experiments conducted to map and *in situ* observe high resolution strain maps at the laboratory of Mechanics of Advanced Materials in Boğaziçi University. The chosen images are of surfaces at microscopic scales to provide additional challenge and to implicate higher scientific importance.

These image pairs that show different deformation and surface pattern characteristics are analyzed using a DIC algorithm that is built purely in Python from scratch [41]. The algorithm is purposefully written in an extensible manner to easily allow different implementations in image and data processing, and optimization functions that would be used in recursive passes to recover otherwise lost data. The bulk of the codes for the algorithm can be found in a remote online repository [42].

2. ADAPTIVE DIC ALGORITHM

With adaptive DIC, this study refers to an algorithm that iteratively attempts to fix erroneous DIC optimization results. Adaptive DIC algorithm, shown in the Figure 2.1 below, consists mainly of two stages. In the first stage, a regular DIC analysis with a coarse-to-fine optimization scheme is carried out over a pre-processed image pair. Second stage, which is the main contribution of this thesis, is a recursive correction cycle that attempts to reduce faulty strain measurements. Outliers from the first analysis are detected; new initial guesses are constructed for all faulty points (by interpolating nearby successful points), and another pass of fine optimization is implemented to correct them. The recursive stage can be repeated a desired number of times. Also, if desired different set of parameters can be used or the iterations can be terminated if remaining spoiled data points are identified to be irrecoverable, guided with the provided measures of quality.

2.1. Regular DIC Analysis

This part of the algorithm shares many elements with the common DIC algorithms (although many specific elements of the described DIC analysis can easily be modified here), which is the reason why the "regular DIC" moniker is used here. In this work, regular DIC is a subset based, two-dimensional DIC algorithm that consists of a pre-processing step to process inputted images, a novel coarse-search algorithm to accurately guess the deformation vector for each data point at a predefined analysis grid, a fine-search algorithm that refines the deformation vector, and a function to calculate strains. The correlation coefficient used fine-search is adapted from Vendroux (1998), which is in the form of $C(f(x,y), g(\tilde{x},\tilde{y}) - w)$, where w denotes the average out-of-plane displacement [25], since the images used in that work are obtained from scanning tunnel microscopy (STM), which measures surface topography. However, the images analyzed in this thesis are captured by an optical microscope and therefore each pixel value denotes the intensity of light at that pixel. As a result, w becomes a measure of average gray-level change in a subset. Together with deformation parameters, the

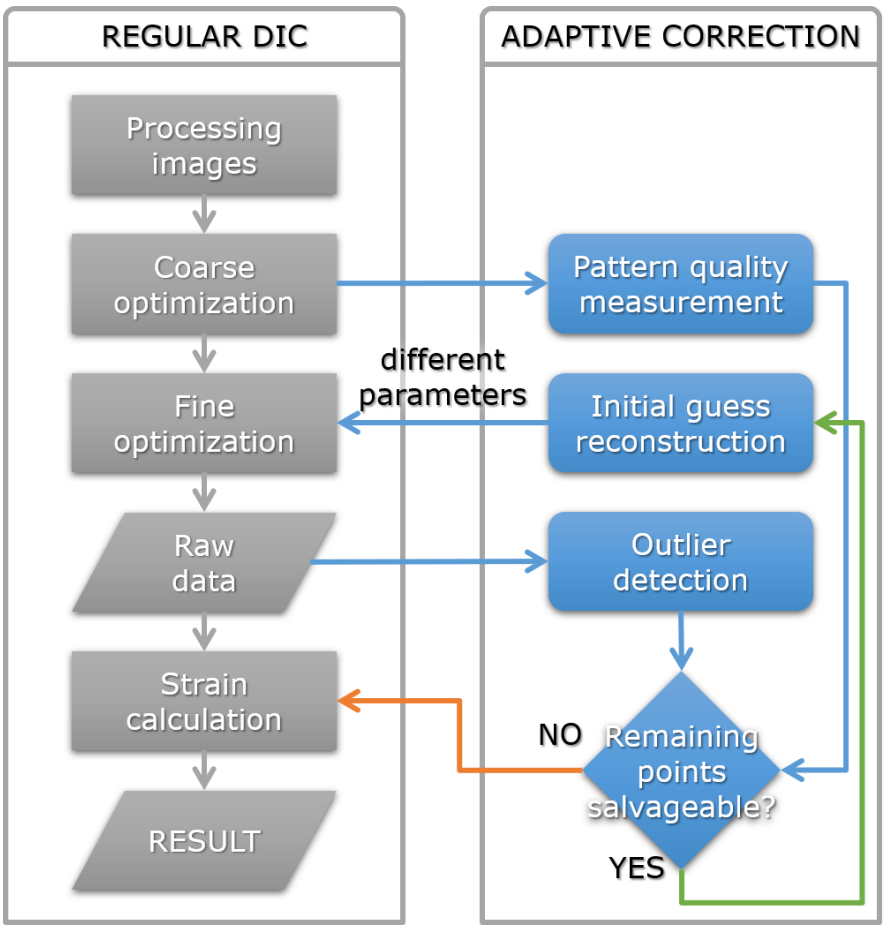

Figure 2.1. Flowchart of the adaptive DIC algorithm, depicting the relation of the proposed adaptive correction with the regular DIC.

solution to the correlation becomes a seven-dimensional vector $P(u, v, u_x, u_y, v_x, v_y, w)$. The rationale behind using the 7^{th} parameter along with the rest of the algorithm, will be explained in the following subsections.

2.1.1. Processing of images

Reference and deformed images are processed before DIC analysis. Both are filtered with a low-pass filter in order to reduce high-frequency image noise (Figure 2.2) [43]. Denoising images will help both reduce bias errors due to poor interpolation and increase the performance of the optimization since the high-frequency noise, which is normally amplified when taking derivatives, is smoothed out [8,16]. For

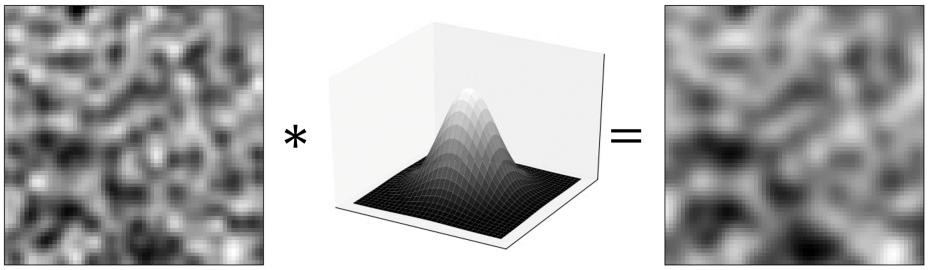

Figure 2.2. Gaussian filtering. Image is convolved with a (dome-shaped) Gaussian kernel to filter-out high-frequency noise.

this purpose, Gaussian filters with standard deviations between 0.75–1.25 pixels are recommended [44]. To avoid removing too much high-frequency data along with noise, in this work, a rather small, 3×3 Gaussian filter with a standard deviation of 0.8 pixels is used to denoise images for all test cases. Gaussian filter is applied with the built-in image processing routines of scikit-image package [45].

2.1.2. Coarse optimization

In this algorithm, each data point is treated separately to reduce any directional bias that may arise from a fixed calculation path. Also, a crude sense of overall deformation is needed to calculate pattern degradation which will be explained in Section 2.2.1.1. Therefore, a cascaded displacement registry method similar to Xavier (2012) is implemented to estimate an independent but accurate initial guess for each data point in the analysis grid [46].

Proposed coarse search method starts by calculating the cross-correlation r between reference and deformed images, I and J:

$$r = \mathcal{F}^{-1}\{\mathcal{F}(I)^* \odot \mathcal{F}(J)\} \tag{2.1}$$

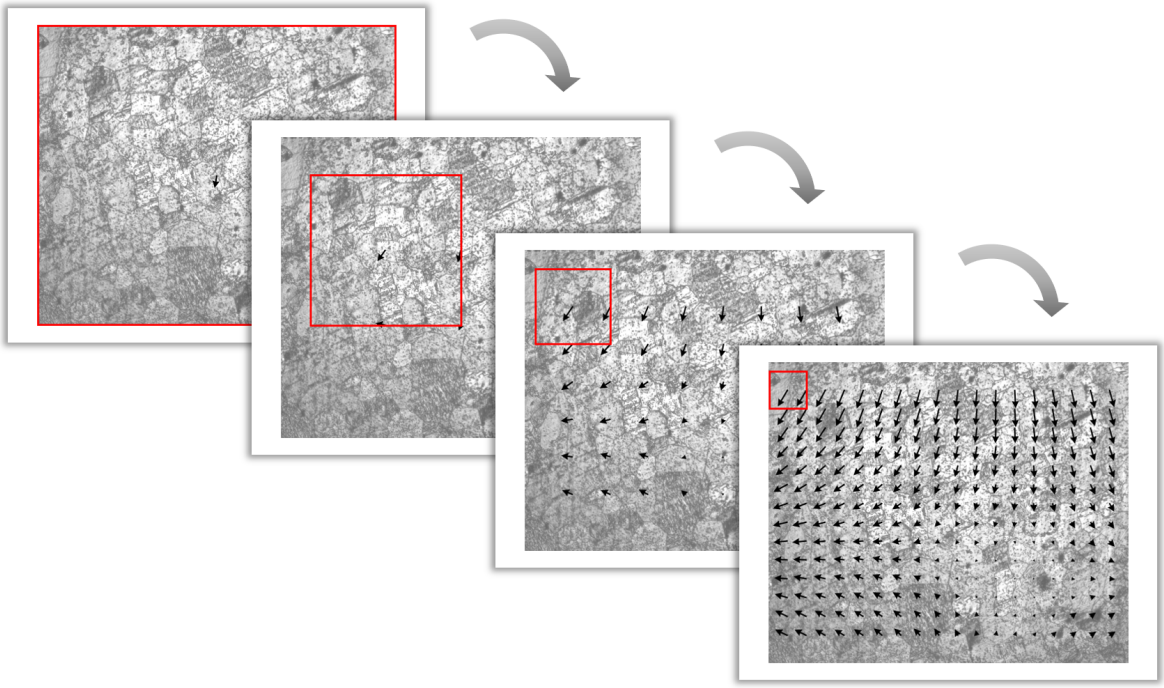

Figure 2.3. Cascaded displacement registry method. Red rectangles indicate the extent of search regions and black arrows point to calculated displacement directions at that iteration. Displacement magnitudes are exaggerated for clarity.

where $\mathcal{F}$ denotes discrete Fourier transform (DFT), * denotes complex conjugation, and $\odot$ denotes element-wise multiplication. Here, location of the peak value of cross-correlation matrix will yield the overall integer shift (u, v) of the image:

$$(u, v) = \arg\max\{r\} \tag{2.2}$$

After the overall displacement is obtained, a small (low resolution) temporary analysis grid with large subsets is formed. Grid spacing, d, is selected as a quarter of the shortest image dimension, while subset size is $(2d + 1)$. Displacement values calculated in the previous step are used as initial guess of deformed subset coordinates, and for each subset, displacement values are calculated using Eq. 2.1 and Eq. 2.2 as implemented the scikit-image package [45]. A median filter is applied to both of the resulting displacement fields to mitigate the effects of possible errors in displacement registry from carrying over to subsequent operations. Afterwards, this process con-

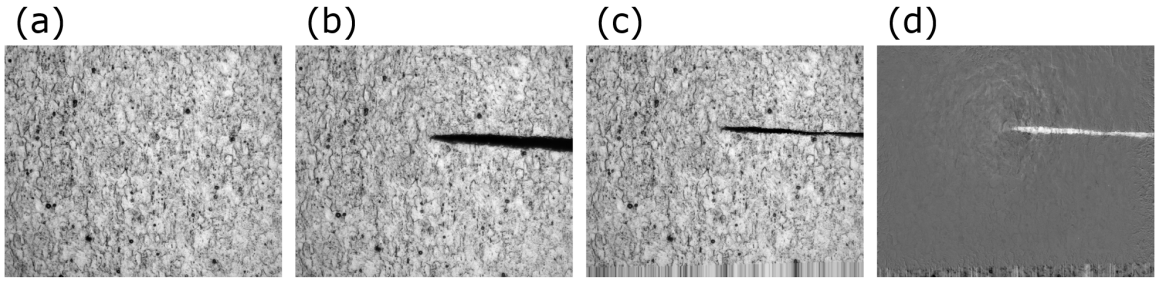

Figure 2.4. (a) Reference image. (b) Deformed image. (c) Deformed image under approximate reference configuration. (d) Change in gray-level intensity. Nearest neighbor interpolation is used to fill values that fell outside the bounds of images.

tinues iteratively by halving grid spacing (and thus, subset size) at each iteration, and setting the initial guess as the displacement value of the nearest grid point of the previous iteration. Figure 2.3 depicts the procedure explained here.

The iterations are proceeded until grid spacing becomes at least equal to the half of the DIC subset size M_{sub}. This termination criterion is necessary to ensure there are at least 3 points with known displacement values within any DIC subset, because that is the minimum number of points needed to specify an affine transformation (first order deformation matrix).

The points with the calculated displacement values that lie within a DIC subset are fed into an OpenCV implementation [47] of the RANSAC (random sample consensus) algorithm [48]. RANSAC first randomly samples at least 3 displacement values (hypothetical inliers), fits them to an affine transformation, and tests the remaining displacement values (possible outliers) against the calculated affine transformation. The algorithm iterates this procedure until the estimated affine transformation is good enough, and a sufficient number of displacement values are in consensus. At this stage, all six deformation parameters of the seven-dimensional initial guess are calculated.

Require DIC subset size M_{sub}

Compute (u_0, v_0) of I and J using Eq. 2.1 and Eq. 2.2

$[\mathbf{u}_{list}, \mathbf{v}_{list}] \Leftarrow (u_0, v_0)$

Form a grid with a spacing $d = \min(n_{cols}, n_{rows})/4$;

if $d > w_{subset}/2$ **then**

  for (x_0, y_0) in grid, (u, v) in $[\mathbf{u}_{list}, \mathbf{v}_{list}]$ **do**

    $f = f(x_0, y_0)$;

    $g = g(x_0 + u, y_0 + v)$;

    Compute $(\Delta u, \Delta v)$ of f and g using Eq. 2.1 and Eq. 2.2

    $[\mathbf{u}_{list}, \mathbf{v}_{list}] \Leftarrow (u + \Delta u, v + \Delta v)$

  end for

  Apply median filter to $\mathbf{u}_{list}$ and $\mathbf{v}_{list}$

  $d \Leftarrow d/2$

end if

return $\mathbf{u}_{list}$ and $\mathbf{v}_{list}$

for (x_0, y_0) in grid **do**

  Get (u_i, v_i) that fall into $f(x_0, y_0)$

  $P_0(u, v, u_x, u_y, v_x, v_y, 0) \Leftarrow RANSAC(u_i, v_i; x_0, y_0)$

end for

Compute J', deformational reverse of J

$W = I - J'$

for (x_0, y_0) in grid **do**

  Get w_i that fall into $f(x_0, y_0)$

  $P_0(u, v, u_x, u_y, v_x, v_y, w) \Leftarrow \overline{w_i}$

end for

Figure 2.5. Cascaded coarse search algorithm.

To calculate the remaining 7^{th} parameter w, using an interpolated map of discrete displacement values, the deformation of the deformed image is "reversed" to bring each

pixel in the deformed image to their supposedly original configuration in the reference image. Subtracting this deformational reverse image from the reference image will give an approximation of the pixel-by-pixel change in gray-level intensity (see Figure 2.4). Values within a DIC subset is averaged to get the overall shift in gray-level of that subset. This value, together with the six deformation values calculated in the previous step, forms the initial guess. The entire coarse search algorithm is summarized in Figure 2.5.

2.1.3. Fine optimization

In fine optimization, the difference between reference and deformed subset patterns are measured using a modified normalized mean squared error (NMSE) correlation coefficient in the form of:

$$C = \frac{\sum \left[f(x,y) - (g(\tilde{x},\tilde{y}) - w) \right]^2}{\sum f^2(x,y)} \tag{2.3}$$

which can be expressed in terms of the solution vector P as:

$$C(P) = \frac{\sum \left[f - g(P) \right]^2}{\sum f^2} \tag{2.4}$$

If the optimization method is chosen to be Newton-Raphson method as in Eq. 1.5, then the Jacobian of $C(P)$ will be in the form of:

$$\left. \frac{\partial C}{\partial P_i} \right|_{i=1,\ldots,7} = -\frac{2}{\sum f^2} \sum [f - g(P)] \frac{\partial g(P)}{\partial P_i} \tag{2.5}$$

and the Hessian of $C(P)$ will be:

$$\begin{aligned} \left. \frac{\partial^2 C}{\partial P_i \partial P_j} \right|_{i,j=1,\ldots,7} = & -\frac{2}{\sum f^2} \sum [f - g(P)] \frac{\partial^2 g(P)}{\partial P_i \partial P_j} \\ & + \frac{2}{\sum f^2} \sum \frac{\partial g(P)}{\partial P_i} \frac{\partial g(P)}{\partial P_j} \end{aligned} \tag{2.6}$$

if P is close to the real solution, then the following approximation can be made:

$$g(P) \approx f \tag{2.7}$$

which will also simplify the Hessian in Eq. 2.6 into:

$$\left.\frac{\partial^2 C}{\partial P_i \partial P_j}\right|_{i,j=1,\ldots,7} \approx +\frac{2}{\sum f^2} \sum \frac{\partial g(P)}{\partial P_i} \frac{\partial g(P)}{\partial P_j} \tag{2.8}$$

Using the Jacobian in Eq. 2.5 and the approximated Hessian in Eq. 2.8 transforms the optimization function into a Gauss-Newton optimizer, which will still follow the same structure shown in Eq. 1.5. It also has similar convergence characteristics, even though it is computationally less expensive.

A visual of the fine-optimization iterations was already provided in Figure 1.3. At each iteration, an incremental deformation is calculated using Eq. 1.5 and added to the current guess. The new estimation will be used as a guess in the next iteration and so on. The iterations will successfully terminate when either:

(i) norm of the Jacobian vector drops below a tolerance value ϵ_{tol} that is close to zero (the derivative of the function is close to zero)
(ii) the change in deformation vector between two consecutive iterations is smaller than a tolerance value ϵ_{tol} (no significant progress is made)

The optimization scheme fails when:

(i) the norm of the Jacobian vector increases during the iterations (solution diverges from the minimum)
(ii) the changes in deformation vector during the iterations are too large (overshoots the minimum)
(iii) the number of iterations reaches to a predefined maximum n_{iter}
(iv) Some pixels of the deformed subset fall beyond the interpolated region (blue squares in Figure 1.3)

Over the course of the optimization, pixels of the deformed subset are mostly located in non-integer coordinates. These pixel values are interpolated from neighboring pixels that are in integer coordinates using bi-quintic (5^{th} order) B-splines. The interpolated region around the deformed subset is usually kept small enough to lower the computational cost as interpolation is computationally the most expensive part of DIC method. Here, both optimization and interpolation algorithms are written with the use of the respective Python routines in SciPy package [49].

2.1.4. Strain calculation

The optimization result contains six deformation parameters, but only displacements (u, v) are used in strain calculations. Remaining parameters (displacement derivatives) are treated as auxiliary optimization parameters and are discarded here.

Spatial displacement derivatives for a subset located at i^{th} row and j^{th} are recalculated by central-differences method over displacement fields:

$$(u_x)_{i,j} = \frac{u_{i,j+1} - u_{i,j-1}}{2d} \tag{2.9a}$$

$$(u_y)_{i,j} = \frac{u_{i+1,j} - u_{i-1,j}}{2d} \tag{2.9b}$$

$$(v_x)_{i,j} = \frac{v_{i,j+1} - v_{i,j-1}}{2d} \tag{2.9c}$$

$$(v_y)_{i,j} = \frac{v_{i+1,j} - v_{i-1,j}}{2d} \tag{2.9d}$$

where d is the spacing between adjacent subsets. If the in-plane strains and rotations are assumed to be small, they can be calculated using the following equations:

$$\epsilon_x = u_x \ , \quad \epsilon_y = v_y \ , \quad \epsilon_{xy} = \frac{1}{2}(u_y + v_x) \ , \quad \omega_{xy} = \frac{1}{2}(u_y - v_x) \tag{2.10}$$

2.2. Adaptive DIC Correction

This part of the adaptive DIC algorithm mainly focuses re-running the DIC optimization on data points where the optimization results are faulty to reduce the data loss as much as possible. Besides the corrective functions the algorithm also provides useful metrics to predict and identify possible inaccurate optimization results.

2.2.1. A-priori quality measures

Before proceeding further to fine optimization, some information about the patterns in the corresponding subsets is gathered. Two different metrics are proposed here: "pattern degradation", which is a measure of how a pattern is corrupted after the surface is deformed; and "pattern entropy" (not to be confused with subset entropy of [11]), which is a measure of how much information a pattern contains. These measures will be useful in predicting data points that may possibly fail and can be used decisively to disregard data points of unsuccessful optimizations.

2.2.1.1. Pattern degradation. The change in average gray-level value in a subset is assumed to be an indicator of pattern degradation. But this cannot be used directly, since the change in gray-level value can be both positive (increased brightness) and negative (decreased brightness), and there may be systematic sources that cause an overall shift in brightness. Hence, a normalization is needed. The pattern degradation D_i of i^{th} subset is calculated as follows:

$$D_i = |w_i - \tilde{\mu}_w| \tag{2.11}$$

where $\tilde{\mu}_w$ denotes the median of gray-level shift in all subsets as computed in coarse optimization.

2.2.1.2. Pattern entropy. In a study, Fazzini *et al.* (2010) demonstrated that image encoding (in bits) and strain measurement errors are inversely correlated [50]. From

this finding it can be deduced that information content of a pattern is directly correlated to DIC measurements. The information content S_i within a subset can be found by calculating its Shannon entropy [51]:

$$S_i = -\sum_j p_j \log_2 p_j \tag{2.12}$$

where p_j denotes the probability of occurrence of j^{th} pixel within i^{th} subset. For reference, in an 8-bit image (gray-levels ranging from 0 to 255), maximum theoretical pattern entropy of any subset larger than 16×16 is 8 bits.

It should be noted that this metric does not take the possible changes (degradations) in the deformed pattern into account and calculates the quality measures solely for the reference subsets.

2.2.2. Outlier detection

DIC analysis of challenging image sets are most likely to produce failed optimization results. These points can easily be masked out in strain maps since the optimization algorithm notifies its state of success. However, the accuracy of the "successful" optimizations is not known at that stage. As explained in Section 1.3 some anomalies in strain maps can give hints of erroneous DIC measurements, but manually locating and tagging them is not feasible, especially for large data sets. Therefore, a method that automatically locates outlier points is needed.

Outlier by definition (in the context of this work), is a statistical observation that differs significantly from the rest of the samples. So, it would be reasonable to flag strain measurements that deviate the most from the average as outliers. But usually, due to the inherent deformation mechanisms of inspected materials, the strains themselves show varied characteristics, so it would be infeasible to treat the set of data points as a whole. For that reason, data set is required to be divided into groups of similarly deformed data points. The grouping is done using k-means clustering [52]

with the help of routines provided by scikit-learn package [53].

The k-means clustering divides a given data set automatically into k number of clusters. The clustering algorithm first randomly selects k different centroids from the data set and assigns each remaining data point to the group that it is the closest to in terms of its Euclidian distance from the centroids. After each data point is assigned to a cluster, the cluster centroids are updated, and data points are re-assigned to the clusters they are closest to. This process continues until the centroid locations move less than a specified tolerance threshold.

The accuracy of clustering depends highly on the initial centroid coordinates. Therefore, to ensure correct clustering, the clustering process is repeated several times (10 times in this work) with different initial centroid coordinates. Among these runs, the clustering exhibiting the least amount of total variation is chosen to be the best result.

Clustering is conducted with respect to displacement derivatives u_x, u_y, v_x, v_y only. Displacements u, v are not included because they do not exhibit enough meaningful deformational variation to be used in grouping process. Average change in gray-level w is also not included because it is not a measure of deformation, but a byproduct of it. In a study focused on identifying twin formations within grains, Chen and Daly (2018) used k-means clustering with respect to calculated strain values $\epsilon_x, \epsilon_y, \epsilon_{xy}$ [54]. This option is also ruled out in this thesis since their values depend on measured displacements of neighboring data points, of which their accuracy is being the main question here.

Each clustering parameter is also standardized beforehand in itself, using z-score defined as:

$$z_i = \frac{x_i - \mu_x}{\sigma_x} \tag{2.13}$$

where x_i is a clustering parameter value, μ_x is the parameter mean, σ_x is the parameter standard deviation, and z_i is the standardized value (or z-score) of the clustering parameter. As a result, each parameter set will have zero mean and unit standard deviation. The standardization evens out the importance of displacement derivatives used as clustering parameters and rounds up their distribution in the four-dimensional space. This is particularly important as k-means clustering tends to cluster data "isotropically" in each parameter dimension.

After the data set is clustered, data points that lie outside of a range from their respective cluster centroids are discarded until all remaining elements of each cluster are within that range (the range is chosen to be $\pm 4\sigma$ for each cluster). Discarded data points are marked as outliers.

The number of clusters, k, can be directly selected as 1, if the expected deformation of the material is small. If this is the case, outliers are the points that deviate the most from the analysis average. For more complex deformations, the number of clusters can be manually selected if the number of deformation states is known. Otherwise, a separate analysis is to be carried out to select the ideal cluster count. If a_i is the average distance between i^{th} point and the remaining points in its cluster, and b_i is the distance from i^{th} point to its next nearest cluster centroid, then:

$$s_i = \frac{b_i - a_i}{\max\{a_i, b_i\}} \tag{2.14}$$

is the silhouette coefficient for that point. Silhouette coefficient quantifies how close a point to other points in its cluster and how far away that point from its neighboring clusters [55]. A silhouette coefficient close to $+1$ signifies that the data point is far from other clusters, while a silhouette coefficient close to -1 signifies the data point is too close to other clusters and it probably is incorrectly assigned to its current cluster. Optimal cluster amount is determined by selecting the clustering result with the highest average silhouette value, after running k-means algorithm with several different number of clusters. In this work, silhouette analysis is done with cluster numbers varying between 2–6.

Silhouette analysis is done only at the end of the first fine optimization step, and the same optimal cluster number is used throughout consecutive DIC analyses, to reduce computation time. This approach can be considered valid as long as no drastic change occurs in the overall state of the measured deformation.

2.2.3. Reconstruction of initial guesses

Initial guesses of the data points that are flagged as failures or outliers are reconstructed before corrective optimization is carried out. The construction is done by interpolating each parameter of P separately from neighboring successful points by 3^{rd} order spline interpolation. Using a high order spline interpolation is expected to provide a better initial condition than path dependent methods used in the literature (it can be said that they use nearest-neighbor interpolation), because it also factors in the change of parameters over the surface.

2.2.4. Corrective optimization

Corrective optimization is similar to the fine-optimization step elaborated in Section 2.1.3, but it is carried only over flagged data points. Corrective optimization can be done with or without changing fine-optimization settings, but for demonstration purposes, three fixed number of corrective passes each with different optimization parameters are performed in this work.

Table 2.1. Optimizational parameters for each corrective pass.

Pass #	**Correlation coeff.**	**Optimization method**	**Interpolated region**
0^{th}	NMSE	Gauss-Newton	61×61
1^{st}	NMSE	Gauss-Newton	241×241
2^{nd}	NMSE	Powell	241×241
3^{rd}	SSIM	Powell	241×241

First corrective pass uses the same optimization parameters used in regular DIC, except with a larger interpolated region around the deformed subset. This allows the solution to be sought in a wider search region. Second pass again uses the same correlation coefficient, but instead of Gauss-Newton method, Powell's method, which is a derivative-free optimizer that uses repeated single-variable minimizations over conjugate directions (Figure 2.6), is used [56]. Finally, the third pass also changes the correlation coefficient to SSIM (structural similarity). Changes for each corrective pass are summarized in Table 2.1.

Structural similarity is an image quality metric that assesses perceptual similarities between two images [57]. It compares images in terms of their luminance (l), contrast (c), and structure (s); and it is in the form of:

$$SSIM(f,g) = l(f,g)^{\alpha} c(f,g)^{\beta} s(f,g)^{\gamma} \tag{2.15}$$

where:

$$l(f,g) = \frac{2\mu_f\mu_g + c_1}{{\mu_f}^2 + {\mu_g}^2 + c_1} \ , \quad c(f,g) = \frac{2\sigma_f\sigma_g + c_2}{{\sigma_f}^2 + {\sigma_g}^2 + c_2} \ , \quad s(f,g) = \frac{\sigma_{fg} + c_3}{\sigma_f\sigma_g + c_3} \tag{2.16}$$

Taking α, β, γ as 1 and setting $c_3 = c_2/2$, Eq. 2.15 reduces to:

$$SSIM(f,g) = \frac{(2\mu_f\mu_g + c_1)(2\sigma_{fg} + c_2)}{({\mu_f}^2 + {\mu_g}^2 + c_1)({\sigma_f}^2 + {\sigma_g}^2 + c_2)} \tag{2.17}$$

where μ and σ denote the mean and the standard deviation; and σ_{xy} denotes the covariance between f and g. c_1 and c_2 are stabilizers added to prevent the denominator from getting close to zero. They are chosen as:

$$c_1 = (k_1 L)^2 \ , \quad c_2 = (k_2 L)^2 \tag{2.18}$$

with $k_1 = 0.01$, $k_2 = 0.03$, and $L = 255$ (for 8-bit images).

The formula given in Eq. 2.17 is usually applied over a preferably weighted, small window that slides over images (images in this context are subsets). The overall similarity between any two images is obtained by taking the average of SSIM values calculated at every position. A similarity index close 1 means the images are similar; this value is subtracted from 1 to get the dissimilarity index [58], in order to use it in minimization algorithms. The 7^{th} parameter is introduced to this correlation function similarly as explained in Section 2.1.

Require initial guess P_0

Set initial search directions ξ_i as unit vectors for $i = 1, \ldots, 7$

for i in $1, \ldots, 7$ **do**

  Find γ_i that minimizes $C(P_i + \gamma_i \xi_i)$

  $P_{i+1} \Leftarrow P_i + \gamma_i \xi_i$

end for

Calculate $\max\{C(P_{m-1}) - C(P_m)\}$ for $1 \leq m \leq n$

$\Delta \Leftarrow C(P_{m-1}) - C(P_m)$

$C_1 = C(P_0)$

$C_2 = C(P_7)$

$C_3 = C(2P_7 - P_0)$

if $C_3 \geq C_1$ or $(C_1 - 2C_2 + C_3)(C_1 - C_2 - \Delta)^2 \geq 0.5\Delta(C_1 - C_3)^2$ **then**

  Use previous directions $\xi_1, \ldots, \xi_7$

  $P_0 \Leftarrow P_7$

else

  $\xi = P_7 - P_0$

  Find γ that minimizes $C(P_7 + \gamma\xi)$

  Use directions $\xi_1, \ldots, \xi_{m-1}, \xi_{m+1}, \ldots, \xi_7, \xi$

  $P_0 \Leftarrow P_7 + \gamma\xi$

end if

Figure 2.6. Powell's method for multivariate minimization.

3. EXPERIMENTAL DATA

This work focuses on four different test cases that aim to highlight optimization failure modes introduced in Section 1.3. The images used in these test cases are obtained from in-lab experiments of Mechanics of Advanced Materials laboratory in Boğaziçi University. Material surfaces are photographed using an optical microscope mounted on an automated staging mechanism that *in situ* scans the entirety of the surface area under varying tensile or compressive loads. At every load point, the mechanism captures around 100 images of 5 megapixels resolution that add up to $\sim$ 300 megapixels when stitched together. Among these images, only a single frame is selected and analyzed. The properties of the selected images for every test case is summarized in Table 3.1.

Table 3.1. Summary of image and material properties for each test case.

Test Cases	**Material**	**Resolution**	**Explanation**
Case 1	Mg AZ31	$1.977 \times 10^{-4} mm/px$	Insufficient pattern information due to large paint speck
Case 2	NiTi	$1.977 \times 10^{-4} mm/px$	Pattern degradation due to crack propagation
Case 3	Mg AZ31	$8 \times 10^{-5} mm/px$	High deformation gradient due to twinning activity
Case 4	Mg AZ31	$8 \times 10^{-5} mm/px$	Same as Case 3 but with poor initial guesses

Throughout the test cases, a rectangular, equally spaced (10 px spacing) data grid of 30225 data points that spans over the images is used. Optimizations are carried out on subsets with a size 31×31 pixels and first-order mapping functions at each data point. The subpixel values of deformed image are interpolated using 5^{th} order splines.

4. RESULTS

4.1. Case 1: Poor Pattern Information

Pattern quality maps depicting of poor pattern information test case are provided in Figure 4.1 below. The reference image has a pattern entropy, S_{avg}, of 6.62 bits, but the value drops below 3 bits where the large paint blotches are located. An interesting thing to note that is that the entropy of patterns around grain boundaries are higher than the average as they increase the information content, while some intra-granular regions (especially relatively larger ones) contain insufficient information compared to the mean the average. The image set belonging to this case experiences minimal pattern degradation; the overall pattern degradation value is slightly below 2.5. The visible degradations (small, green zones at Figure 4.1b) are mostly located on the large shear band.

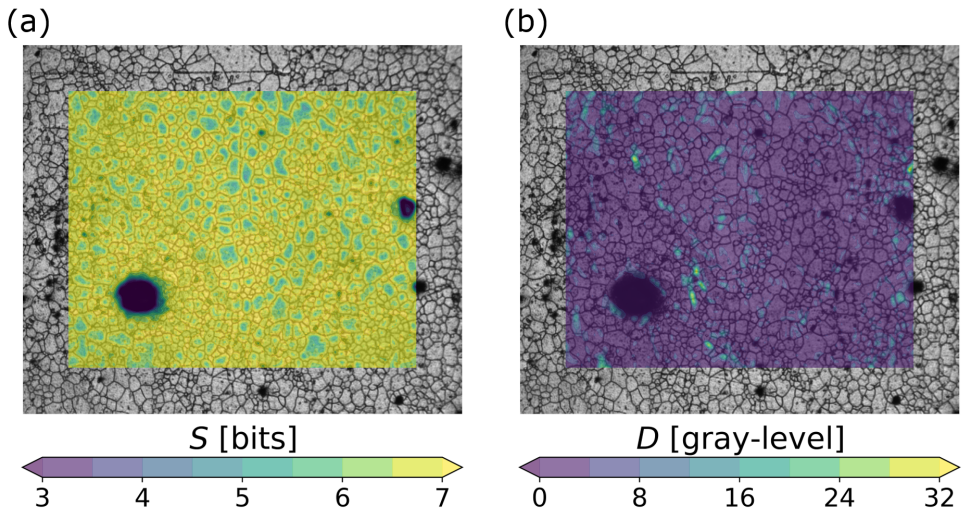

Figure 4.1. (a) Pattern entropy and (b) pattern degradation maps of Case 1, overlaid on reference image.

Silhouette analysis for this case (Figure 4.2) yields the optimum number of clusters as 2 with an average silhouette score of 0.66. For this cluster count, there is one

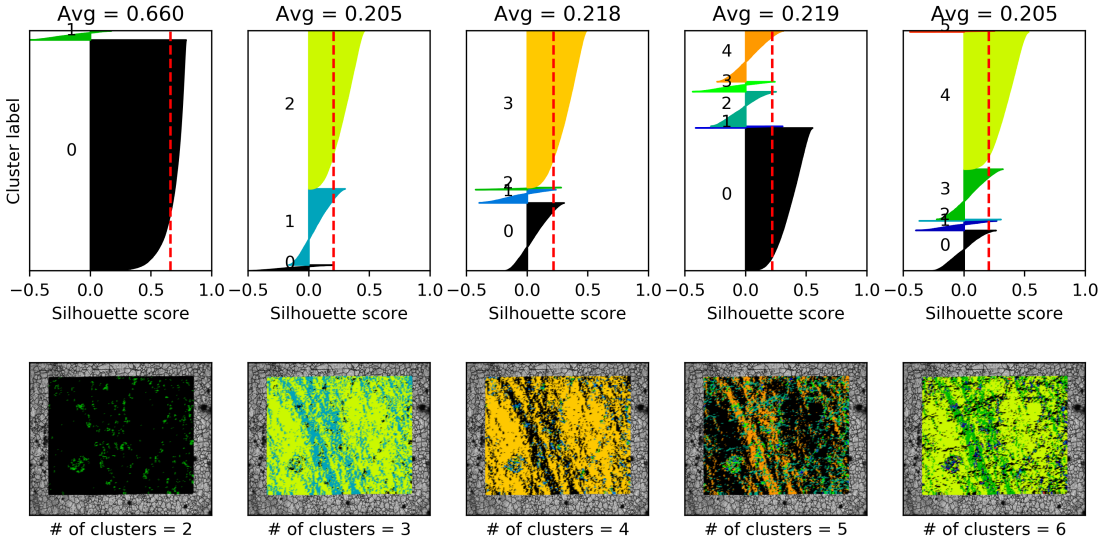

Figure 4.2. Silhouette analysis for Case 1.

large cluster that encompasses most of the analysis field, and a small one in which the data points are located mostly at poor pattern quality regions. It should be noted that the smaller cluster has a negative average silhouette score, which means it is poorly clustered. This is likely to originate from the discrepancy of strain states of possible outlier points that cannot be sensibly placed in any clusters. Clustering results with 3 or more clusters appear to place data points on shear bands into a separate cluster, but these seemingly deformation-aware clusters do not yield optimum results according to the average silhouette scores.

Initial strain measurement over error-free regular DIC optimizations reveals that the material is in tension in y-direction with a median axial strain (ϵ_y) of approximately 1%; but on the shear bands, ϵ_y values can exceed 5% (see Figures 4.3a-b). Out of 30225 data points, regular DIC analysis manages to solve 30165 points, 838 of which are later marked as outliers. As seen strain and pattern quality maps in Figure 4.3, a large number of failures along with some outlier data points are accumulated on the large paint speck at the lower left of the image. Remaining faulty points are scattered around on other low entropy or high degradation regions (Figure 4.3c-d). There is minimal fault around the rightmost paint speck.

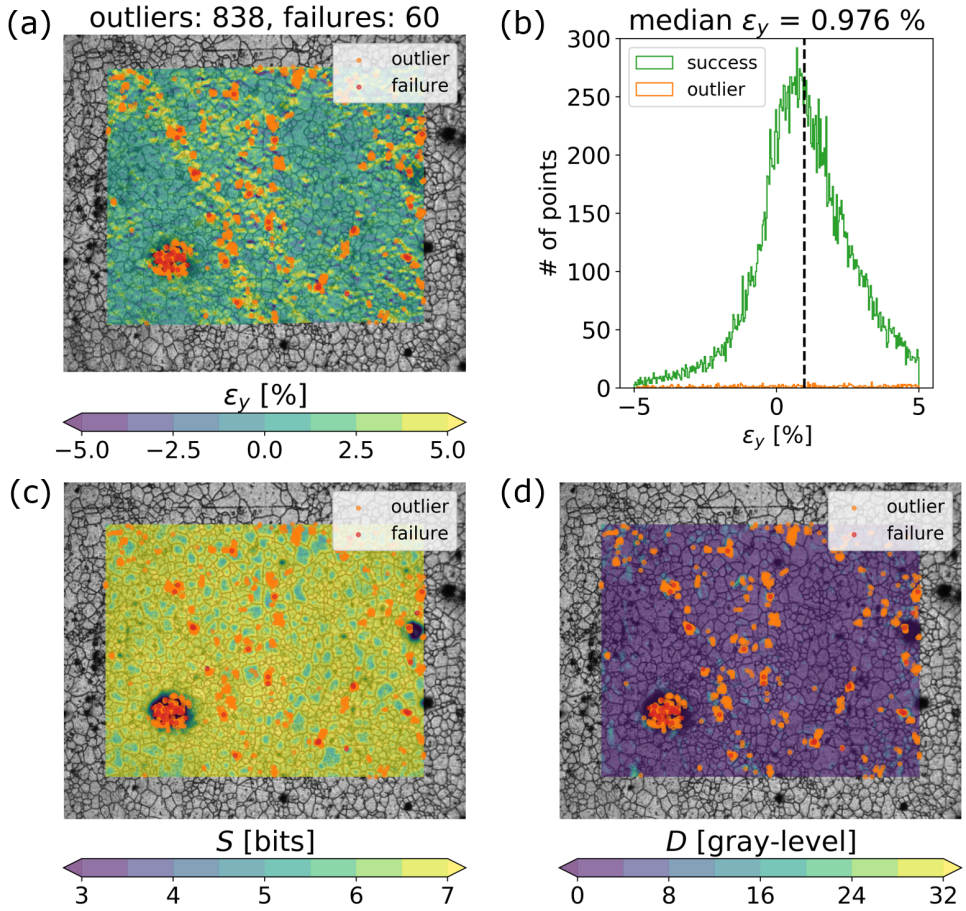

Figure 4.3. Failure and outlier distribution of Case 1 after regular DIC analysis on (a) ϵ_y, (c) pattern entropy, and (d) pattern degradation maps. (b) is the ϵ_y histogram for the same stage.

Passes of adaptive DIC corrections gradually decrease faulty points and even completely eliminate failures in the last corrective pass. Number of outliers also decreases in total (although it goes back up in second pass), but data points on the large paint speck and some other points on the shear bands continue to be marked as outliers (see strain maps of Figure 4.4). Also, it cannot be seen in the strain maps, but strain histograms in Figure 4.4 reveal that with each corrective pass, the tip of the histogram shifts slightly to the right as the median of ϵ_y increases.

Compressing vertical axes to a logarithmic scale and expanding the range of strains in horizontal axes of strain histograms exposes the state of outliers. At each

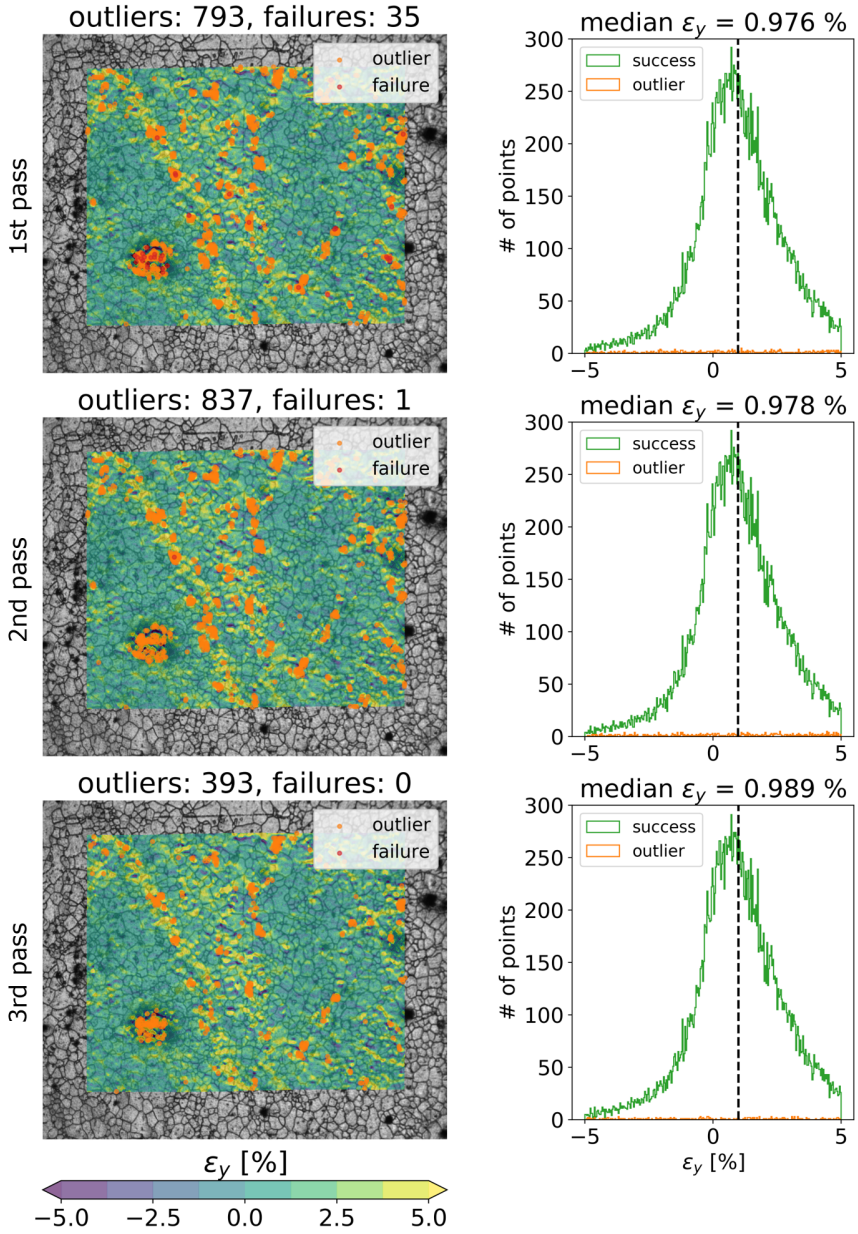

Figure 4.4. ϵ_y maps and histograms of Case 1 after each adaptive correction pass.

DIC stage, there are points with unnaturally high strain values (larger than 25%, as high as 100%) as seen in the skirts of ϵ_y histograms in Figure 4.5. Majority of these high-strain data points are marked as outliers, even though there are occasional misses. On the other hand, a large number of outliers are within the same ±20% strain range as successful data points (that show themselves as small orange curves under narrow green curves).

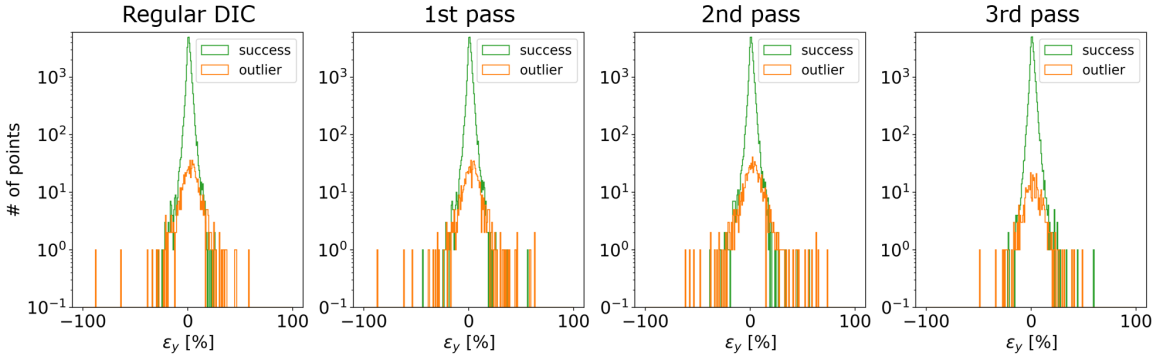

Figure 4.5. ϵ_y histograms of Case 1 in log scale for each DIC stage.

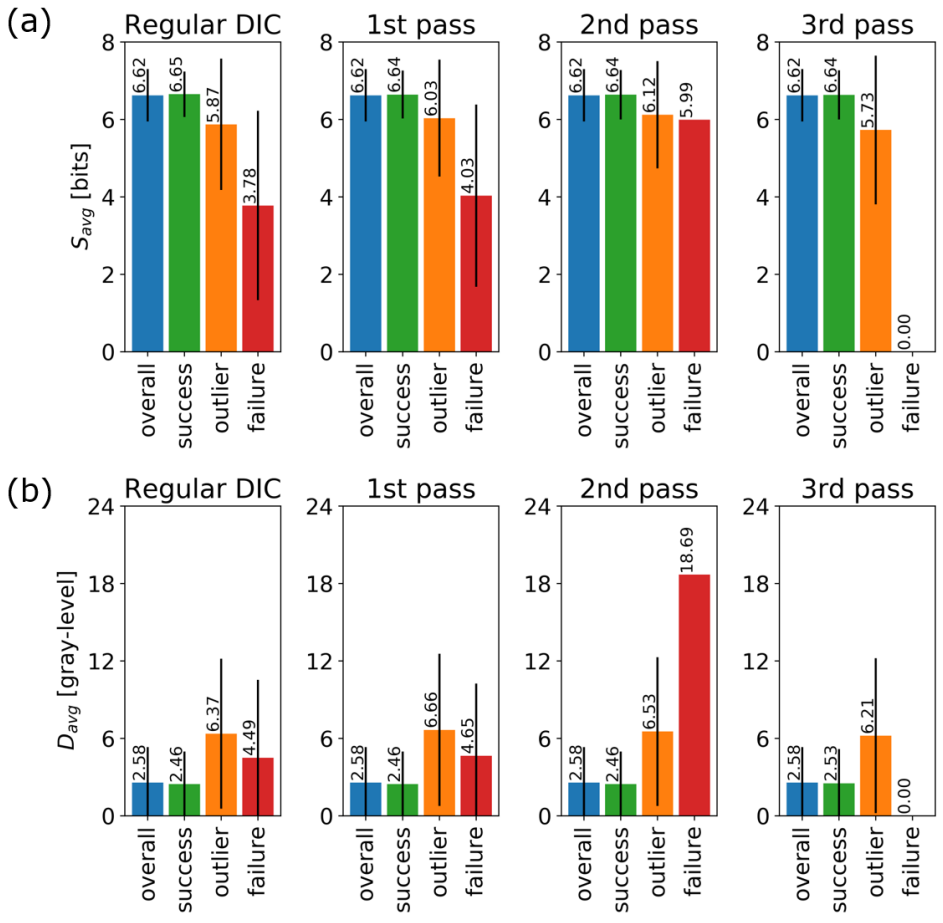

Figure 4.6. Average (a) pattern entropy and (b) pattern degradation charts for data points of Case 1 in different statuses.

The relation between pattern entropy and DIC results can be seen in Figure 4.6a. The image in this test case had an average pattern entropy (S_{avg}) of 6.62 bits overall,

which can be considered high on a scale of 0–8 bits, and the S_{avg} at successful points are even higher than that at every DIC pass. And expectedly, S_{avg} of outlier and failure points are lower than the total average. S_{avg} seem to increase at second corrective DIC pass, but the value shown on the chart belongs to a single remaining failure only. While not being the focus of this test case, the effects of pattern degradation are also visible in Figure 4.6b. In a similar fashion, average pattern degradation (D_{avg}) value of successful points are lower than the overall average of 2.58 gray-levels, while outliers and failures have a higher pattern degradation average. The sudden jump in average D_{avg} at second corrective DIC pass can again be explained by the statistical insignificance of a sole failure point.

4.2. Case 2: Pattern Degradation

The surface of the Nitinol specimen in this test case has an average pattern entropy of 5.64 bits. Other than several tiny specks, there are no obvious features on the surface that might negatively affect the entropy, therefore the entropy distribution within the analysis grid is mostly uniform (see Figure 4.7a). On the other hand,

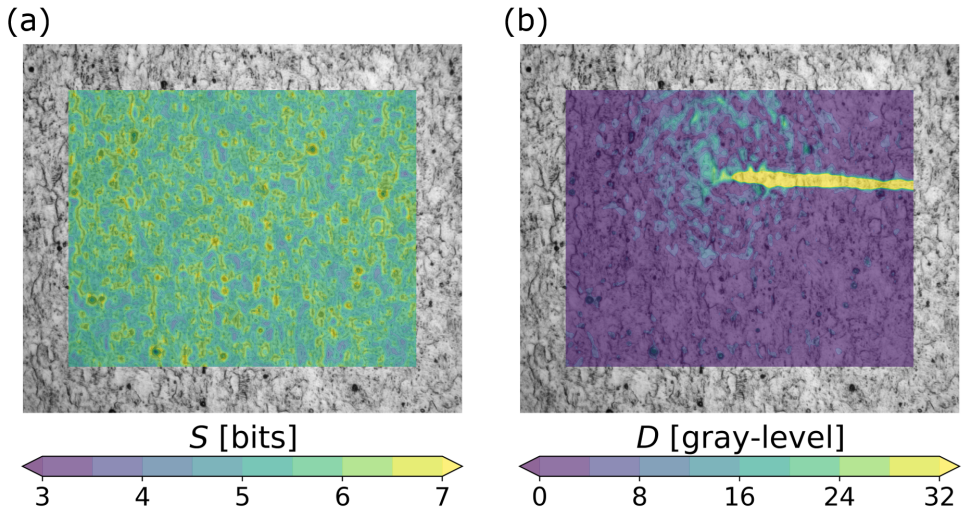

Figure 4.7. (a) Pattern entropy and (b) pattern degradation maps of Case 2, overlaid on reference image.

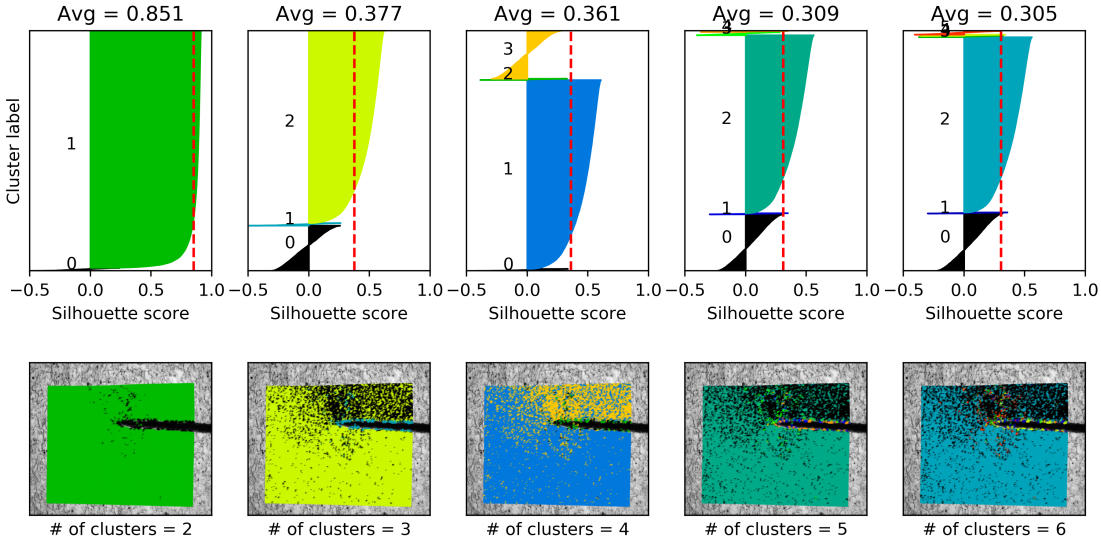

Figure 4.8. Silhouette analysis for Case 2.

the crack that propagates into the deformed image frame causes a significant pattern degradation, which shows up as the yellow horizontal streak as entering from the right edge as seen in Figure 4.7b. Inside this region, pattern degradation values can reach to a maximum of 141 gray-levels. There is also a circular region around the crack tip where pattern degradation is greater than the total average due to excessive deformation.

The highest average silhouette score detected is 0.851 and it corresponds to the case when the number of clusters employed is 2. Similar to the silhouette analysis results acquired in Section 4.1, optimum clustering contains one large cluster and one tiny cluster with a negative average silhouette score. The remaining silhouette analysis results with higher number of clusters are successful in separating the data on two sides of the crack into different groups with relatively higher average silhouette scores, but any other cluster formations than those two, end up in suboptimal configurations with low average silhouette scores and few data points. Cluster distributions and scores for this test case can be seen in Figure 4.8.

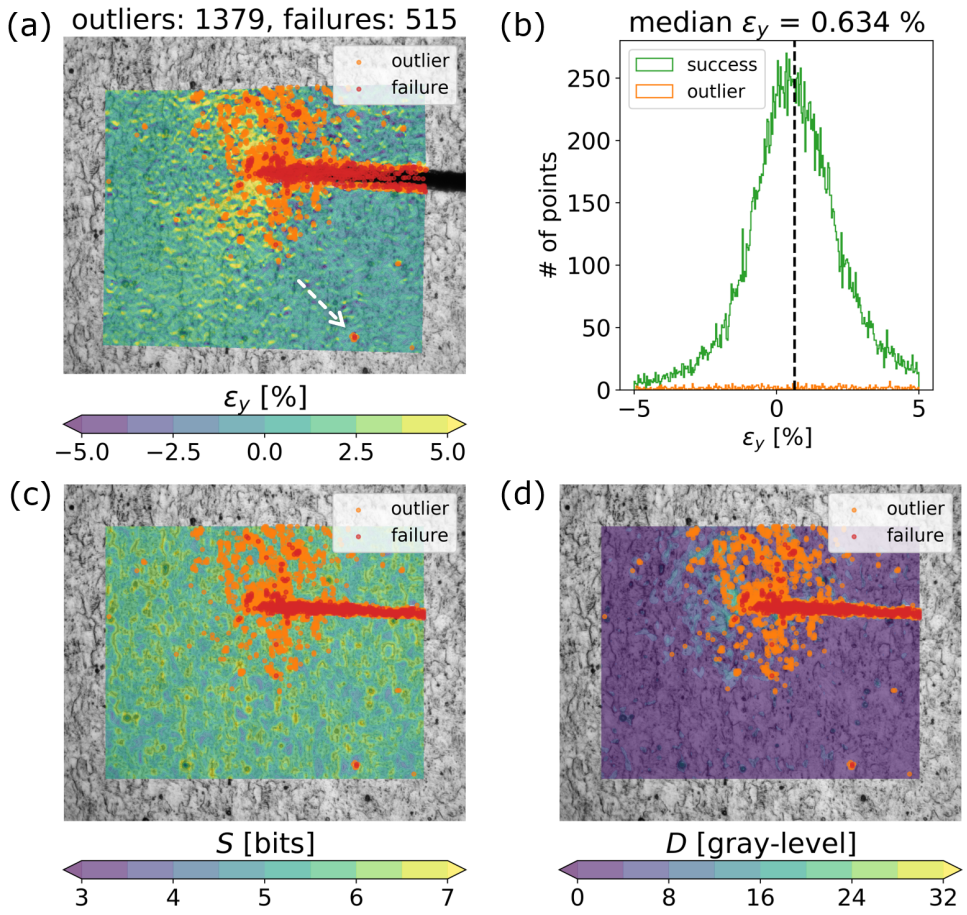

Figure 4.9. Failure and outlier distribution of Case 2 after regular DIC analysis on (a) ϵ_y, (c) pattern entropy, and (d) pattern degradation maps. (b) is the ϵ_y histogram for the same stage.

For this test case, the majority of the 515 failures accumulate around the crack (see Figure 4.9a) and 1379 detected outliers are scattered around areas with high pattern degradation (see Figure 4.9d). A small number of sporadic faults like the small lump of outliers and failures located at the bottom right of the maps (shown with a dashed, white arrow) can also be seen far from the cracked region. No direct correlation between faulty data points and the pattern entropy can be observed from Figure 4.9a. Axial strain histogram in Figure 4.9b shows that the median strain for this test case is 0.634%, but especially around the cracked region the local strain can reach much higher values than that.

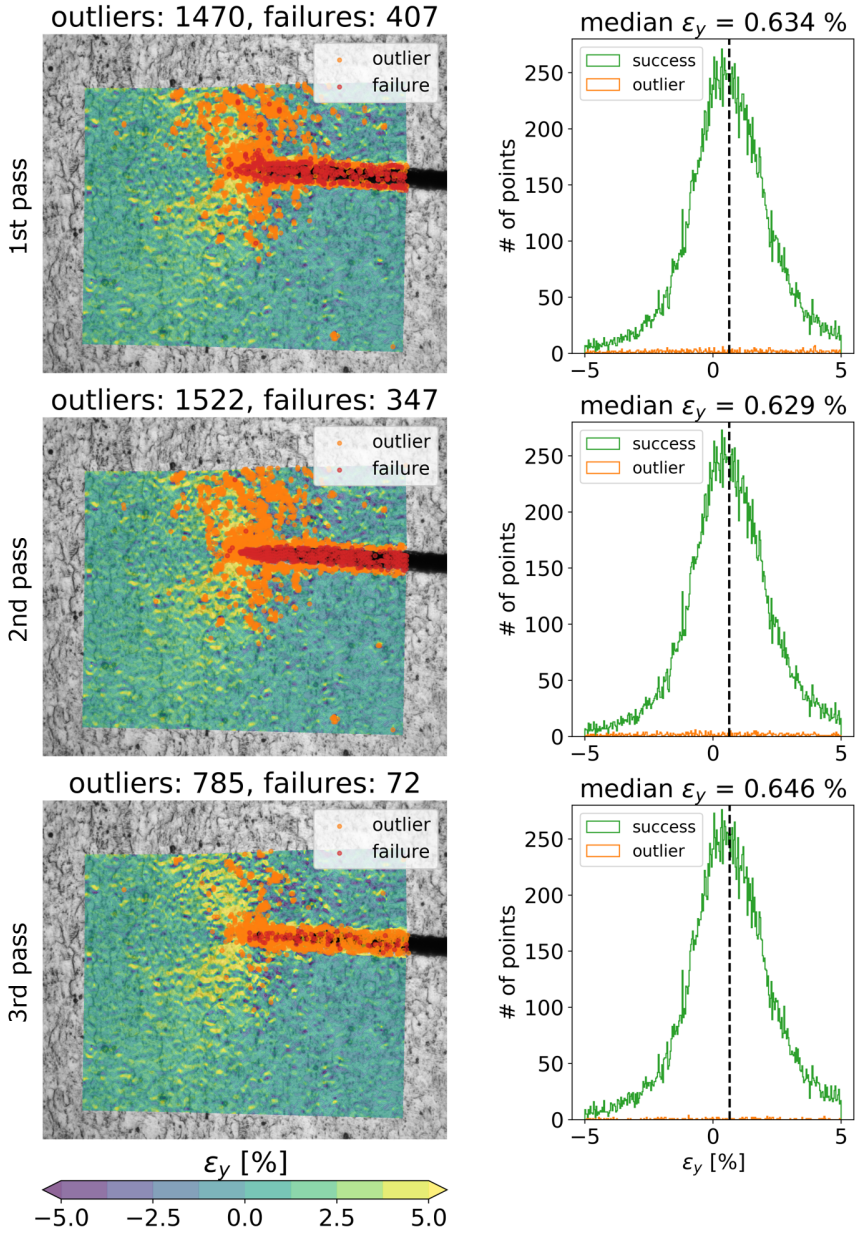

Figure 4.10. ϵ_y maps and histograms of Case 2 after each adaptive correction pass.

Adaptive DIC reduces the number of faulty points at each pass, but the number of solved failure points does not compensate for the increase in successes, since many of the solved points get marked as outliers simultaneously. To illustrate this, by the end of the second pass, 168 of the initial 515 failures are solved, but the number of successful points increase only by 25 (from 28331 to 28356). As third adaptive pass is completed, a considerable amount of improvement is observed such that the ratio of

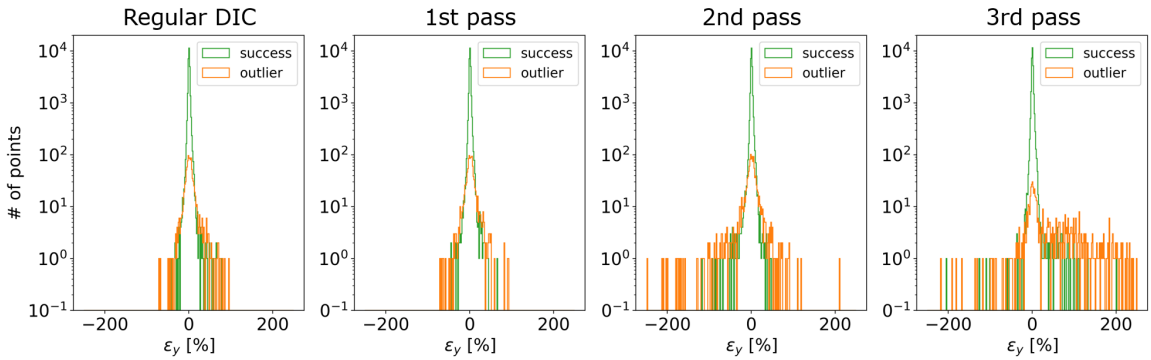

Figure 4.11. ϵ_y histograms of Case 2 in log scale for each DIC stage.

data points with successful DIC measurements increases from 93.7% to 97.2% of the total.

After each adaptive correction iteration, failed data points are localized inside the cracked region, and it reduces into a thin sliver of points at the final corrective pass (see strain maps in Figure 4.10). The final pass also reduces the number of outliers by more than 50%. At this stage, faulty points residing far from the cracked region are mostly recovered. For example, the small lump in the lower right mentioned earlier was cleaned up from failures after the first corrective pass, and finally recovered completely after the third pass. One should further note that strain histograms in Figure 4.10 also shows an overall increase in median ϵ_y value (although not as obvious as it was in Case 1 since the value dips slightly at second pass) throughout adaptive DIC corrections.

Strain histograms with logarithmic y-axes and expanded x-axes (Figure 4.11) verifies the previous remark on decrease in failures being not equal to increase in successes. After each adaptive correction pass, the skirts of ϵ_y histograms widens but with mostly outliers (orange colored curves). Such high axial strain values in the order of 50–250% are strong indicators of divergences in DIC optimizations.

As stated earlier, the distribution of faulty points for this test case did not show any visible correlation with the pattern entropy map, and the average pattern entropy bar chart in Figure 4.12a confirms that statement. S_{avg} for successes are infinitesimally

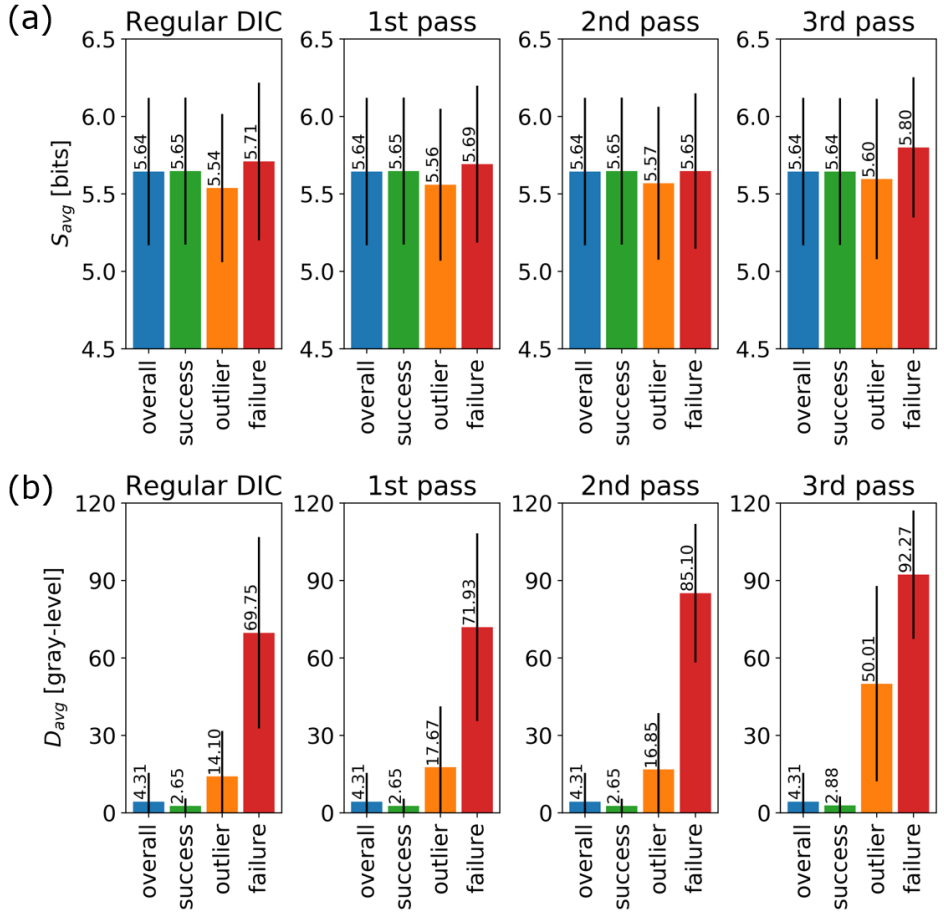

Figure 4.12. Average (a) pattern entropy and (b) pattern degradation charts for data points of Case 2 in different statuses.

higher, and outliers are slightly lower than the overall average (5.64 bits). However, the difference is not significant enough to claim a correlation.

Contrarily, Figure 4.12b shows that average pattern degradation values show such a strong correlation with the state of success that average pattern degradation values for outliers and failures are multiples higher than the overall average (2.65 gray-level). Furthermore, D_{avg} value for faulty points show an upward trend throughout adaptive DIC analyses, while it stays approximately the same for successes. This may indicate that the algorithm recovers the data points with low D_{avg} at each pass.

4.3. Case 3: High Deformation Gradients

Subsets of the chosen reference image for the third case has an S_{avg} value of 6.10 bits overall. Figure 4.13a shows that this value goes higher than the overall average near the grain boundaries, and drops below the overall average inside the grains. There are two specks on the right side of the region of interest, on which the pattern entropy drops significantly. One of the grains that is located at the lower center of the analysis grid (area encircled with dashed white lines in the figure), has a slightly higher pattern entropy than the rest of the image. However, the same grain contains a thick twin band, which causes an excessive pattern degradation at the same area (see the encircled region in Figure 4.13b). Throughout the region of interest, several other twin formations, albeit not as excessive as the encircled one, can also be seen in the pattern degradation map.

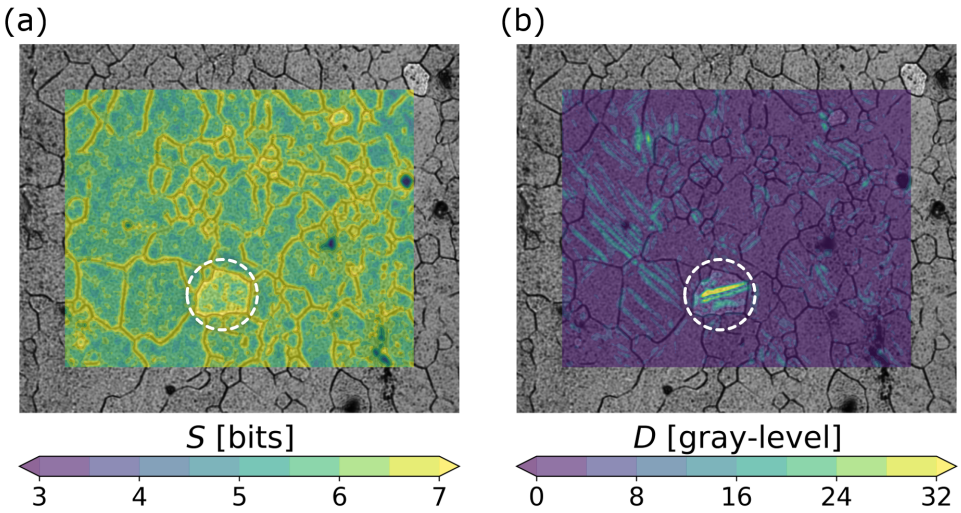

Figure 4.13. (a) Pattern entropy and (b) pattern degradation maps of Case 3, overlaid on reference image.

The data points are clustered into 2 sets, since the average silhouette score is the highest (0.62) at that number; though the clustering with 3 sets have a close average silhouette score (0.614). Both 2 and 3-cluster configurations contain one large cluster with a high silhouette score that includes the majority of the data points, while other

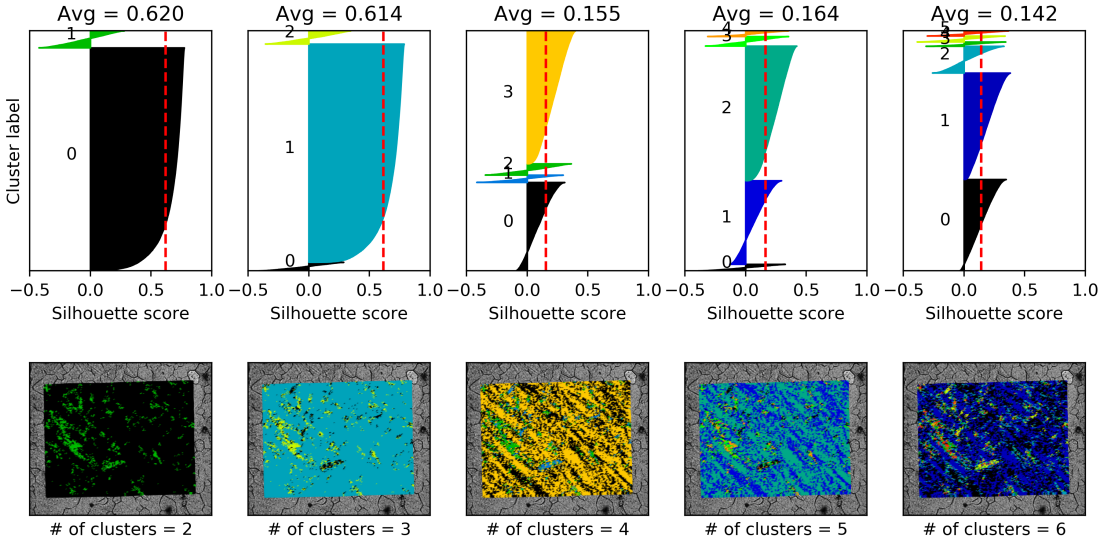

Figure 4.14. Silhouette analysis for Case 3.

clusters are small and have negative average silhouette scores. These small clusters are mostly comprised of data points with highly degraded patterns. Starting from 4 clusters, the larger cluster is also split into multiple clusters by the algorithm. The silhouette analysis results for this test case can be seen in Figure 4.14.

Initial DIC analysis spawns 1527 faulty data points, 454 of which correspond to failures. These faulty data are almost exclusively positioned at twin formation sites with degraded patterns as seen in Figures 4.15a-d. Apart from several outliers around the two black paint specks, no significant correlation with pattern entropy can be observed from Figure 4.15c.

The specimen of this test case is under axial compression, and its median ϵ_y value is slightly below -2% (Figure 4.15b). The multitude of diagonal compressive bands (thin and dark stripes in Figure 4.15a) confirms that the test case has indeed large gradients in deformation, but the overall deformation range is also higher than the previous test cases as the range of strains is used in strain map and histogram is doubled to emphasize the role of the strain state.

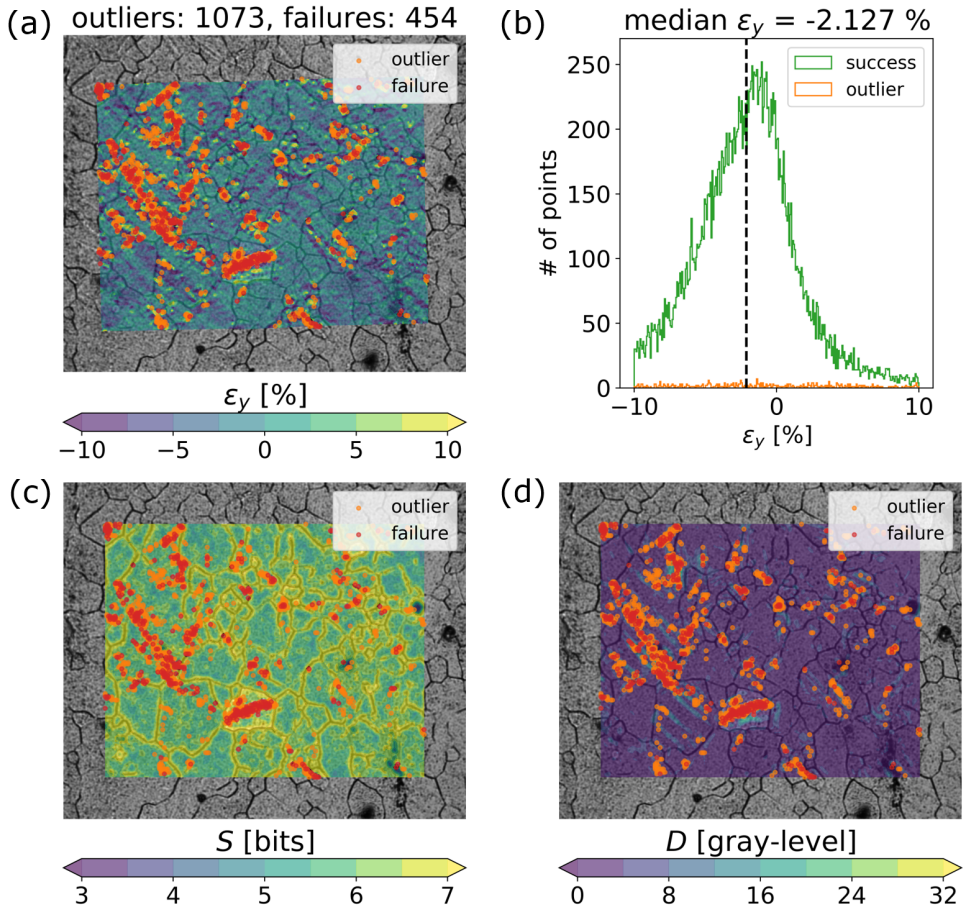

Figure 4.15. Failure and outlier distribution of Case 3 after regular DIC analysis on (a) ϵ_y, (c) pattern entropy, and (d) pattern degradation maps. (b) is the ϵ_y histogram for the same stage.

Adaptive DIC algorithm achieves to steadily reduce the number of faults in this test case at each corrective pass. The largest decrease in failures can be observed in the second pass, where almost 90% of the failures are eliminated (from 316 to 32 failed points). The effect is demonstrated as a reduction of red dots in Figure 4.16. On the other hand, the third pass recovers the greatest number of points (666 faulty points recovered). A large chunk of remaining unrecovered data points still lie on the encircled twin band in Figure 4.13b. Similar to the previous test cases, the tip of the strain histogram shifts leftward at each step as the median of ϵ_y decreases (increases in magnitude).

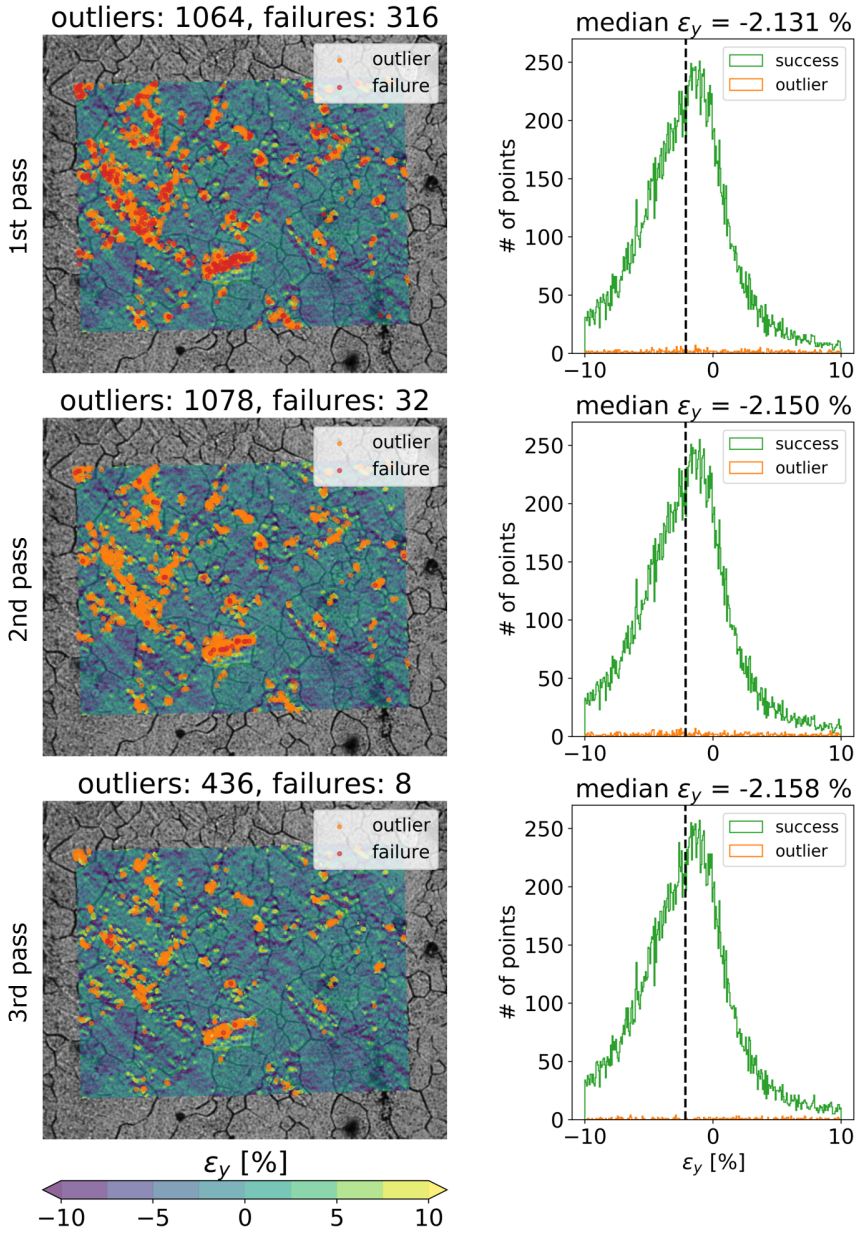

Figure 4.16. ϵ_y maps and histograms of Case 3 with faulty points after adaptive correction passes.

Strain histograms with logarithmic scales in Figure 4.17 validate findings in the previous paragraph. The histograms of regular DIC and the first corrective pass look similar as there is little recovery of the corresponding data. The expansion of the width of the skirts in the second pass shows that the algorithm solved some of the failed points, but most of them are tagged as outliers again. In the third pass, the skirt

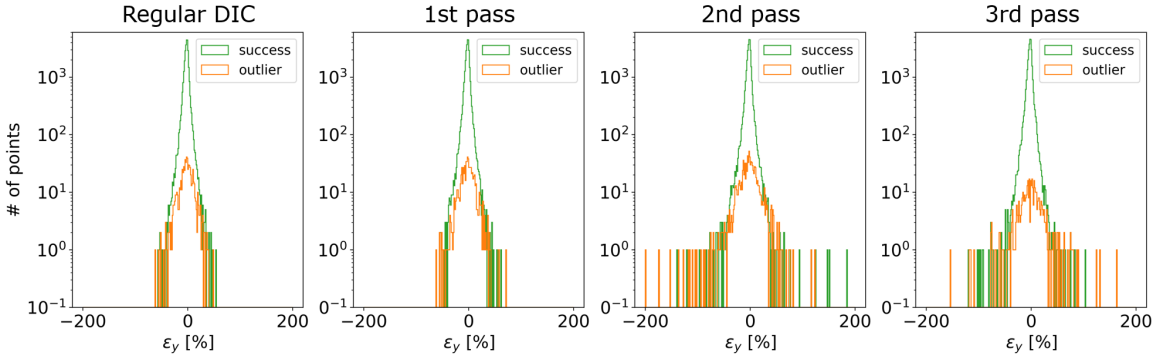

Figure 4.17. ϵ_y histograms of Case 3 in log scale for each DIC stage.

of the histogram curve shrinks a bit as some of the faults recovered; but some points with far-fetched strain values remain and not identified as outliers. The possible reason behind this inefficacy will be discussed in the Section 4.5.

There was no apparent correlation between pattern entropy and DIC optimization results, but the bar chart in Figure 4.18a indicates that there is indeed a correlation (albeit a small one). Points marked as successful exhibit consistently higher S_{avg} values than the overall S_{avg} of 6.10 bits. Likewise, S_{avg} of outliers are lower than the overall average, and S_{avg} of failures are even lower than that. This shows that the effect of the information content within the subsets can manifest itself even within regions dominated by large and high-gradient deformations.

The effects of pattern degradation on DIC measurements can again be seen in Figure 4.23b: successful data points have D_{avg} values lower than the overall average of 3 gray-levels, while outliers and failures have D_{avg} values consistently higher than that. This result is expected as the formation of twins is an excessive deformation mode that also causes an out-of-plane motion. This motion not only alters the surface topography, but also changes the reflectivity of the surface, which degrades the surface pattern.

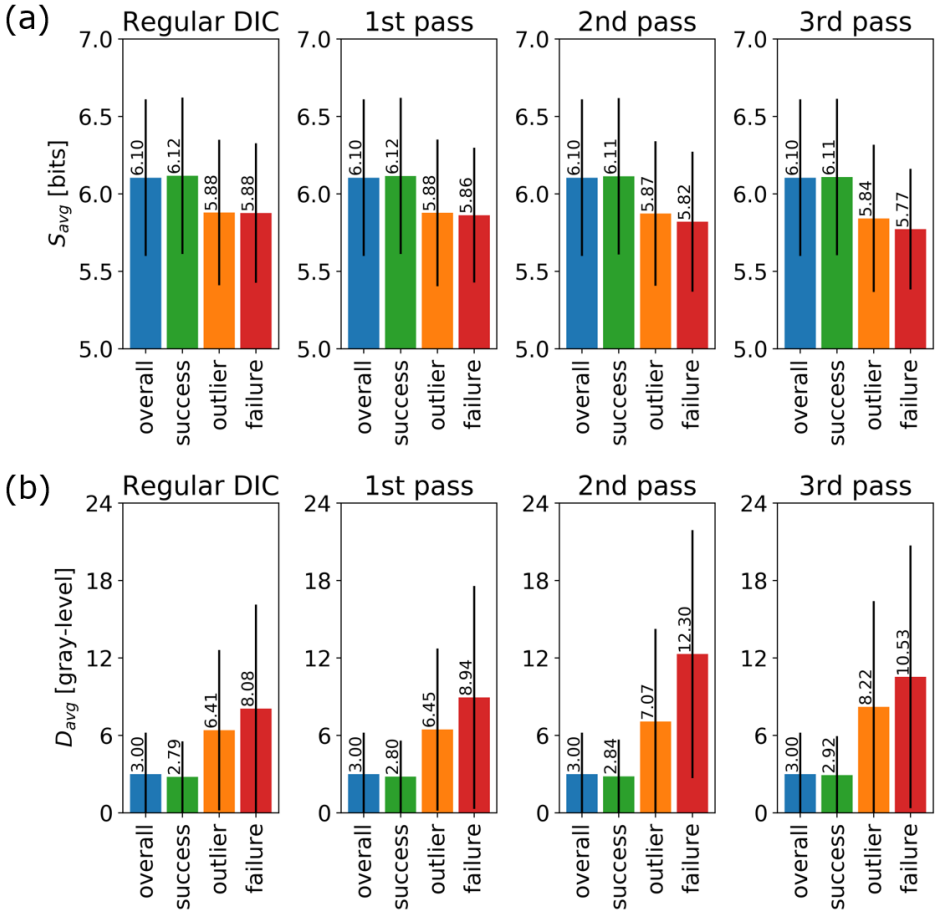

Figure 4.18. Average (a) pattern entropy and (b) pattern degradation charts for data points of Case 3 in different statuses.

4.4. Case 4: Poor Initial Guesses

Case 4 shares image pair that is used in Case 3, therefore the pattern quality maps will be the same as in Figure 4.13. The results of silhouette analysis (Figure 4.19) are also similar to of Case 3, so much so that all remarks made for Case 3 on silhouette analysis are valid here too. This observation supports the assumption made in Section 2.2.2 that the optimum clustering result will remain unchanged throughout consecutive corrective passes if there are no major differences in the measured deformation field.

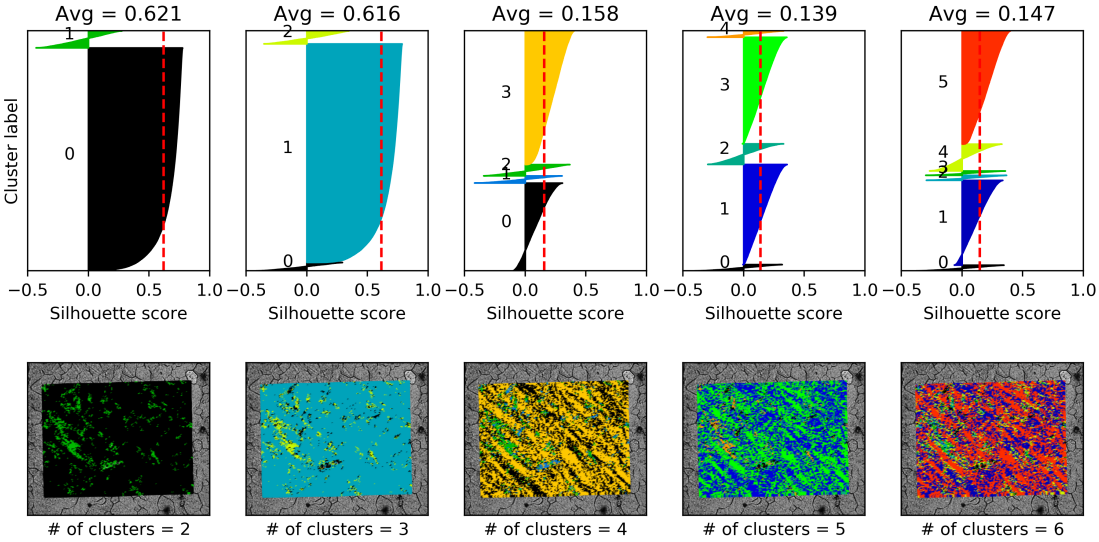

Figure 4.19. Silhouette analysis for Case 4.

Regular DIC analysis results accentuate the differences between this test case and the previous one, though. The amount of failures increases more than 18% with respect to Case 3 (454 failures in Case 3 vs 537 failures in Case 4), because the initial guesses are altered. Remaining solved data points include the same number of outliers. Maps in Figure 4.20 show that the faulty points are distributed similarly over degraded patterns of twinned regions. One thing to note that the median of measured overall axial strain in this step is lower than what was measured in the regular DIC step of Case 3 by 0.2%.

Adaptive DIC passes show a data recovery trend that is also similar to the Case 3. Figure 4.21 shows that the number of failures decrease at each corrective step, while the total number of faulty points exhibits a sharp decrease in the third pass. Measured overall compressive strain increases also similarly during adaptive corrections as seen in ϵ_y histograms. At the end of the DIC analysis, the number of data points with successful optimizations do not exhibit a significant change (in fact, lower than Case 3 by only 24 data points).

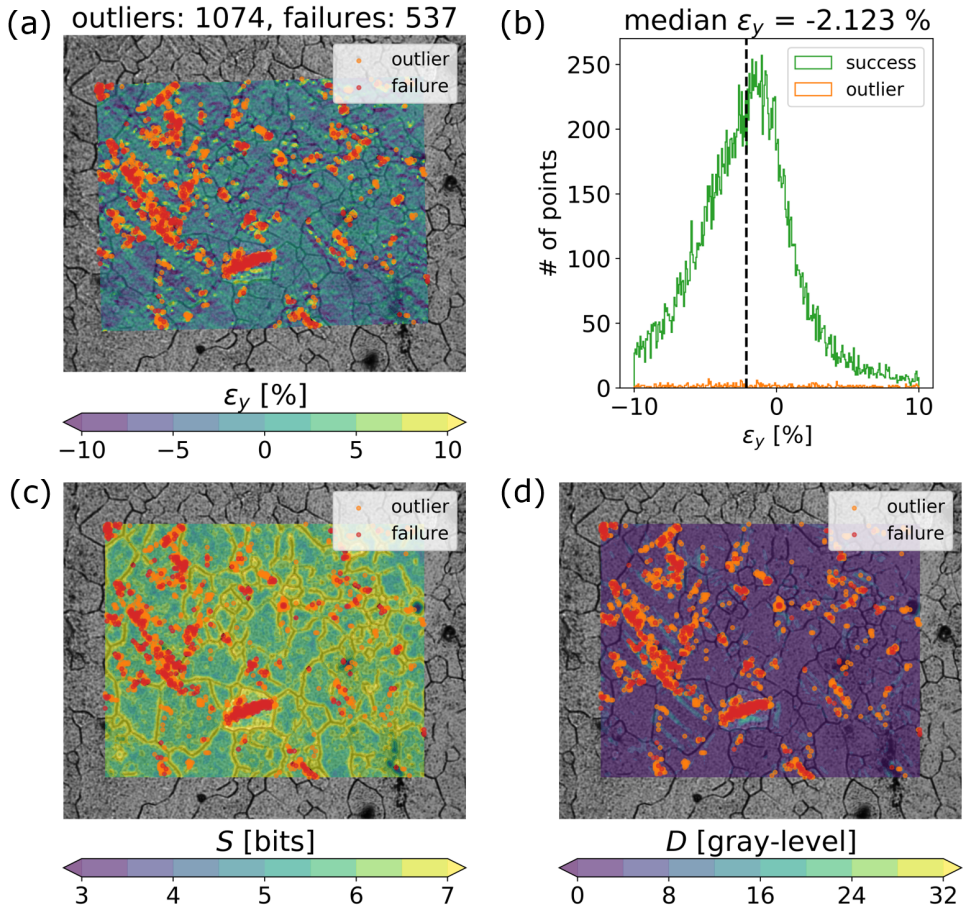

Figure 4.20. Failure and outlier distribution of Case 4 after regular DIC analysis on (a) ϵ_y, (c) pattern entropy, and (d) pattern degradation maps. (b) is the ϵ_y histogram for the same stage.

ϵ_y histograms with logarithmic scales in Figure 4.22 are shown just for demonstration purposes. Other than the skirts of histogram curves contracting back into the $\pm 100\% \epsilon_y$ range at the end of the third pass, no noteworthy remark compared to Case 3 can be made.

Finally, the average pattern quality values for different success states for Case 4 are shown in Figure 4.23. General trend in this work can again be observed here: on average, successful data points have higher pattern quality values (higher S_{avg} and lower D_{avg}) than the overall; in contrast with the faulty points. Contrary to expectations, the average pattern entropy is prone to be higher for failures than for outliers here.

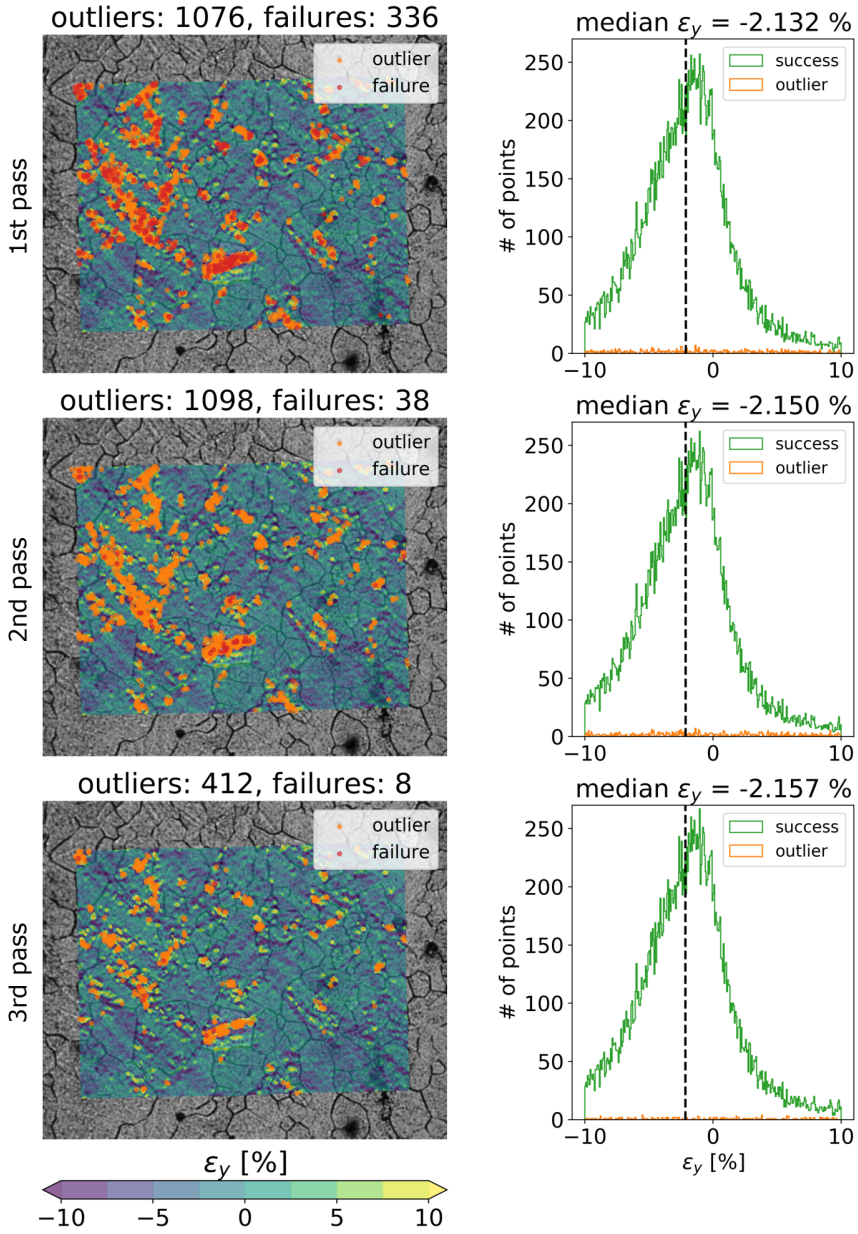

Figure 4.21. ϵ_y maps and histograms of Case 4 with faulty points after adaptive correction passes.

Though, the average pattern entropy does not act as a distinctive indicator by itself to infer an underlying abnormality, since the degradation of patterns affects the success of DIC optimization results more dominantly in this case.

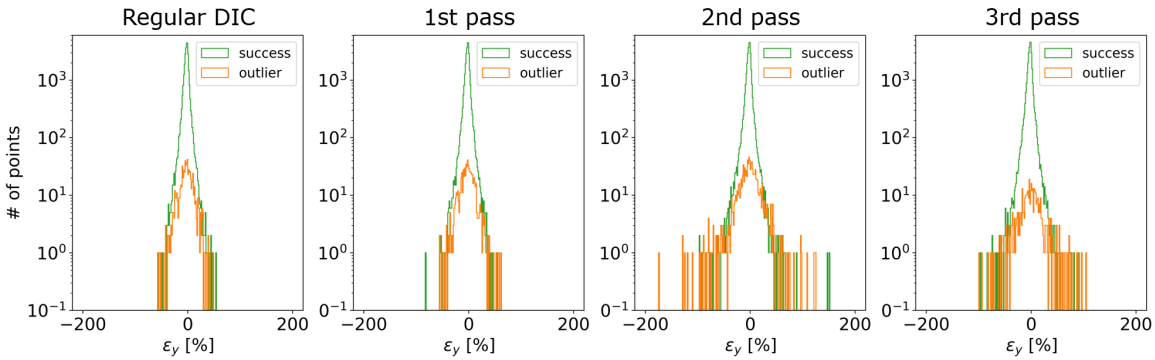

Figure 4.22. ϵ_y histograms of Case 4 in log scale for each DIC stage.

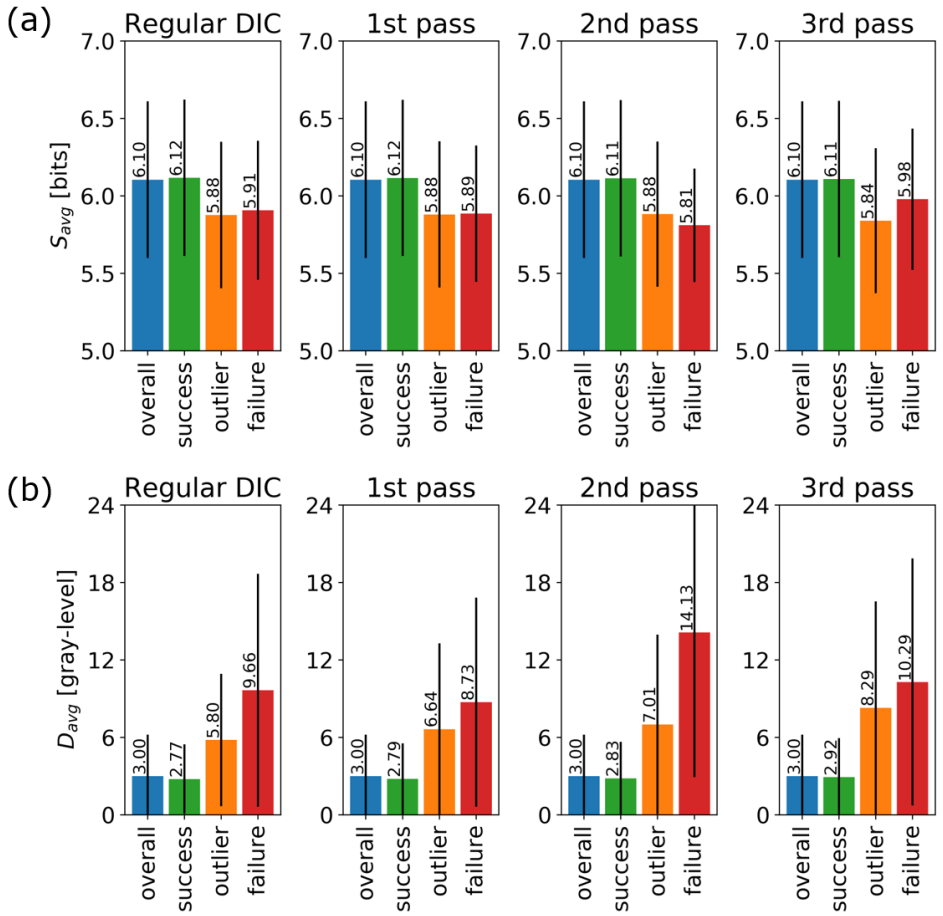

Figure 4.23. Average (a) pattern entropy and (b) pattern degradation charts for data points of Case 4 in different statuses.

4.5. Discussion

4.5.1. Predictive power of pattern quality measures

DIC analyses of all four cases demonstrate that the pattern quality has an impact on the success of optimizations. To quantify this effect, the correlation between each pattern quality measure and the state of success is calculated. If the state of success is introduced as a dichotomous variable (0 means failure or outlier, 1 means success), then the correlation can be calculated using point biserial correlation coefficient [59]:

$$r_{pb} = \frac{\overline{Y_1} - \overline{Y_0}}{\sigma_Y} \sqrt{\frac{n_1 n_0}{n^2}} \tag{4.1}$$

where $\overline{Y}$ denotes the average of the pattern quality measure; σ_Y denotes the standard deviation of the pattern quality measure, n denotes the number of data points, and subscripts 0 and 1 denote the failure and success, respectively. The value of r_{pb} varies in ± 1 range: values of -1 or +1 indicate deterministic relationships, and 0 means no correlation.

Using Eq. 4.1, the heat maps in Figure 4.24 are produced. This figure shows that, for all test cases and DIC stages, optimization success is correlated to pattern entropy and inversely correlated to pattern degradation; although average correlation value for pattern entropy is closer to zero than for pattern degradation. Highest correlation to pattern entropy is observed in Case 1 (poor pattern information case) and highest correlation to pattern degradation is observed in Case 2 (high pattern degradation case), which are in line with the anticipations of this thesis.

Pattern quality has the ability to sway DIC measurements, but the exact effect on the optimization result is hard to predict as all images exhibit different pattern quality properties. Therefore, it is also difficult to specify a clear delimiting quality value for success. Still, this thesis provides valuable data in terms of pattern quality. To find such a threshold value, among all tests, pattern quality values of data points with the lowest pattern entropy $S_{\min}$ and the highest pattern degradation $D_{\max}$ the algorithm

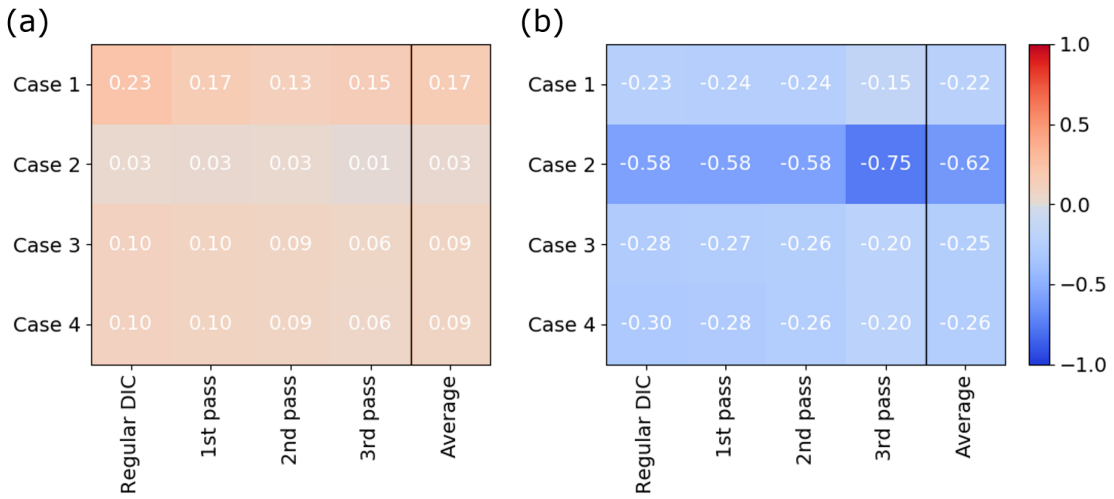

Figure 4.24. Heat maps of correlation between successful optimizations and (a) pattern entropy, (b) pattern degradation.

successfully solves are averaged. According to this calculation, the DIC algorithm can solve data points with pattern entropy values as low as 2.791 bits, and with pattern degradation values as high as 49.576 gray-levels. However, one should note that these values are suggested not as strict thresholds, but as guidance.

4.5.2. Accuracy of outlier detection method

In every test case, strain histograms with logarithmic scales show some abnormally high strain data points that are marked successful. The reason behind this inefficacy is not actually an inefficacy but a discrepancy between methods used in obtaining displacement derivatives. As explained in Section 2.1.4, strains are calculated from spatial displacement derivatives, rather than optimizational parameters. On the other hand, parameters used in k-means clustering, as explained in Section 2.2.2 are optimizational displacement derivatives. As a result, even though a data point is flagged as an outlier, its neighbors can be affected by inaccurate measurements. Figure 4.25 demonstrates the discrepancy between optimizational and spatial displacement derivatives. Notice the absence of green curves in high strain ranges in Figure 4.25a. A possible solution for this can be simply excluding all 4 neighbors of outliers from strain

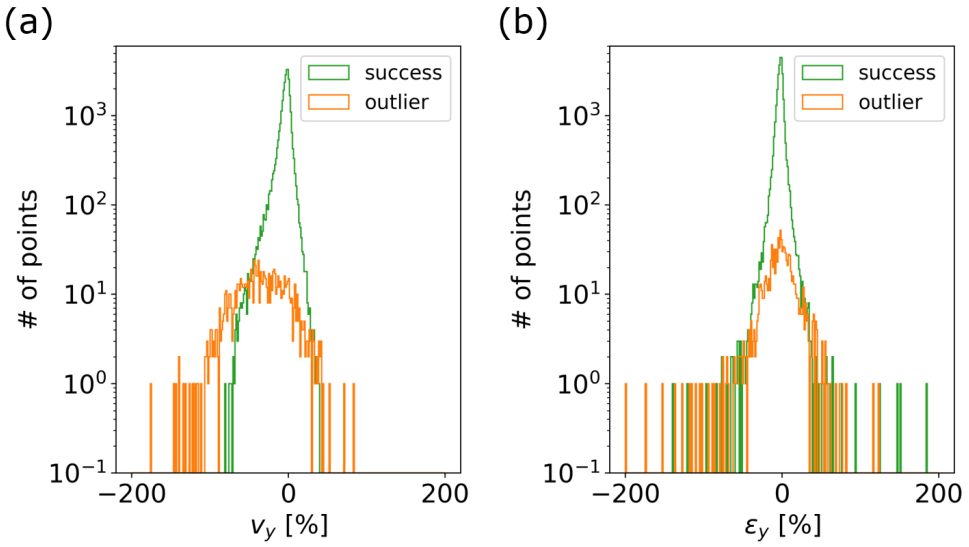

Figure 4.25. Log scaled histograms of (a) v_y and (b) ϵ_y after 2^{nd} corrective pass on Case 3.

histograms.

Figure 4.25 points also to a different problem in outlier detection. Orange colored histogram curves beneath the green ones show that some data points are flagged as outliers even though they exhibit low strains. Actually, it is not scientific to reach an exact conclusion just by looking at these results as state of other strain components are not investigated yet. But if that is still the case, the reason for outliers with low strains can be explained with a conservatively chosen σ value.

On another note, every silhouette analysis in this work produces either a large cluster coupled with small and poor clusters, or several clusters with moderate silhouette scores. These results imply that clusters largely overlap each other and thus data points are not entirely suitable to be clustered with a k-means algorithm. To improve the reliability of outlier detection procedure, a more robust clustering algorithm may be delineated in the prospective studies.

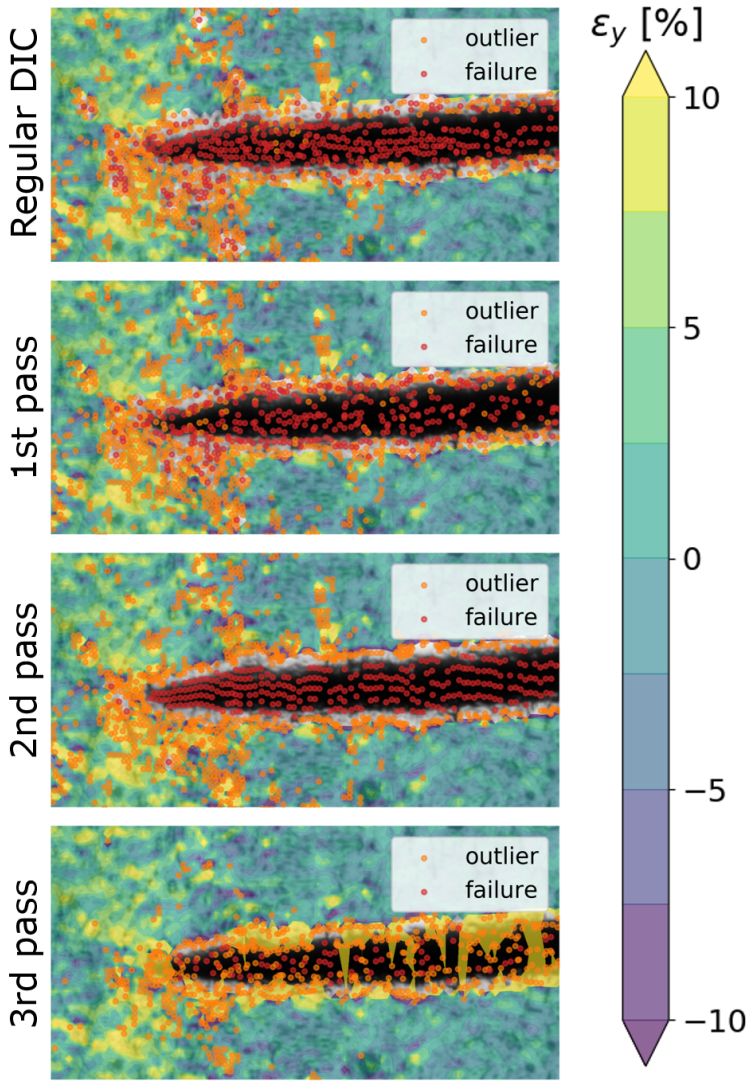

Figure 4.26. A close-up on the crack tip ϵ_y maps of Case 2.

4.5.3. Effectiveness of corrective algorithms

Adaptive DIC algorithm recovers majority of the faulty data at the end of third corrective pass in each test case. As noted earlier in DIC results, overall axial strain values reported by the algorithm increase over each corrective pass, which can be attributed to successful recovery of high strain points that are initially flagged as faulty. However, one should be aware of possible over-fitted optimization results. For example, the close-up strain maps given in Figure 4.26 show that successful optimizations gradually approach to the crack boundary, but at the last step the algorithm over-fits several

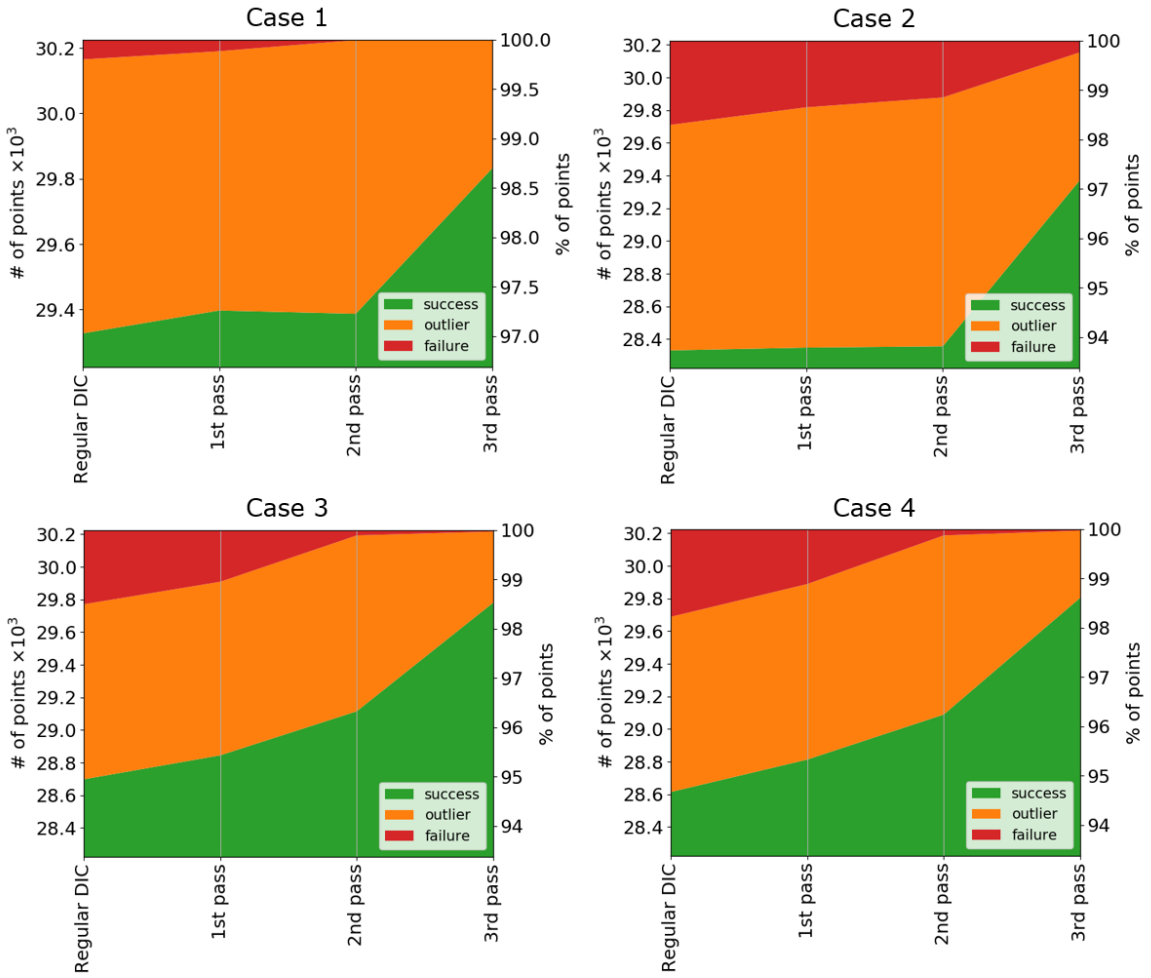

Figure 4.27. Number of points for success states after each DIC pass.

points that lie within the crack gap. These over-fitting results are flagged by outlier detection algorithm, but they still affect neighboring data points due to the way strains are calculated, which creates the jagged appearance in the strain map. As a remedy, these undistinguished points can be possibly discarded later with a thresholding on pattern degradation values.

Among all corrective passes, the number of recovered points culminates in the third pass. This is visualized by the variation in the slope of the domain boundary formed between green and orange stacks in Figure 4.27, as it is the steepest between second and third passes for all test cases. This is likely because of the sophisticated correlation coefficient (SSIM) used in the third pass, but the exact reason is difficult to

pinpoint since there are other variables involved and no controlled tests were conducted. Moreover, the amount of mislabeled data (as shown in Figure 4.26) is unknown.

4.5.4. Effectiveness of the repaired initial guesses

Before each corrective pass, initial guesses of faulty points are reconstructed with the help of newly acquired information. Overall, an improvement in successful DIC optimizations is observed, but it is currently not possible to attribute the success to the repaired initial guesses as there are several other variables too that may have contributed to the outcome.

5. CONCLUSION

Digital image correlation is an indispensable method in high-resolution deformation measurement. To produce deformation maps, a binary set of images of any material surface in undeformed and deformed states are compared subset by subset, with the help of a minimization routine to find the optimum affine transformation that ensures the best fit between each subset pair. Taking the gradient of the obtained displacement field will produce the strain distribution. However, as the measurement scale shrinks towards microscopic length scales, images obtained from optical microscopy introduce several challenges like, more prominent displacement gradients and out of plane displacements, poor pattern signature, difficulty in applying a properly distributed speckle pattern, camera noise etc., which may yield failed or erroneous strain evaluations.

Conventional DIC algorithms seek to achieve an overall best representation of the strain field via a single, (expectantly) good algorithm that reaches the optimum as fast as possible while overlooking any individual complications that may arise from the smallness of the observed scale or the technicalities of the used imaging method. In that case, incorrect DIC evaluations appear and they may be presented alongside accurate results, which hampers the reliability of the strain measurements in general.

This work proposes an algorithm that reevaluates challenging data points in order to correct them. The algorithm uses k-means clustering to group similarly deformed data, marks misfits in each group as outliers, and reruns the optimization process on outliers together with failures. Moreover, two pattern quality measures are proposed, namely, pattern entropy and pattern degradation that aim to predict possible erroneous strain measurements upon a-priori evaluations of information content and the change in overall gray-level of the pattern within subsets, respectively.

Four sets of image pairs, each with varying deformation and pattern quality characteristics are inspected in order to test the validity of the claims of the proposed algorithm. Each test pair is first analyzed with a coarse search algorithm that calcu-

lates the displacements in a cascaded manner and computes affine transformations for each data point using these displacements. Then a DIC algorithm that uses a simple correlation coefficient (normalized mean squared error) and a common minimization method (Newton-Raphson) is used to refine the initial deformation field provided by the coarse search. After outliers are identified, three consecutive, corrective DIC analyses are conducted, each with different (and more costly) parameters. The improvements after each corrective pass are noted in conjunction with pattern quality values.

Analysis results of each test case demonstrate that pattern quality is correlated to the success of the DIC evaluations; successful optimization results have both higher pattern entropy and lower pattern degradation values in general. Proposed outlier detection algorithm successfully marks data points with poor pattern quality and high deformation, independently from the said pattern quality measurements. Finally, it is shown that the number of faulty DIC evaluations can be reduced via different (albeit more costly) corrective DIC algorithms, which is the main purpose of this thesis. In conclusion, the proposed adaptive DIC algorithm works promisingly in terms of increasing the reliability of the measurements, but its quantitative effectiveness on different pattern quality and deformation states remain to be a topic of future studies.

6. FUTURE WORK

The outlier detection algorithm accomplishes to identify poor pattern quality and high deformation regions as possible outliers, but with an unknown accuracy. Controlled experiments with (synthetically produced) images of known deformation states and manually introduced outliers should be used to test the accuracy of the outlier detection algorithm and the feasibility of k-means method in such an outlier detection setting. A comparison of k-means method to other clustering algorithms should also be conducted to find an optimum method to better group similarly deformed data points that largely overlap other clusters.

In a similar fashion, the effectiveness and computational cost of various correlation coefficients and minimization functions over different types of challenging image pairs should be tested and ranked; and the need for a reconstruction of initial conditions should be examined in controlled environments.

REFERENCES

1. Sutton, M. A., J.-J. Orteu and H. W. Schreier, *Image correlation for shape, motion and deformation measurements: basic concepts, theory and applications*, Springer, New York, N.Y, 2009, oCLC: ocn227916898.

2. Pan, B., K. Qian, H. Xie and A. Asundi, "Two-dimensional digital image correlation for in-plane displacement and strain measurement: a review", *Measurement Science and Technology*, Vol. 20, No. 6, p. 062001, 2009.

3. Bing, P., X. Hui-min, X. Bo-qin and D. Fu-long, "Performance of sub-pixel registration algorithms in digital image correlation", *Measurement Science and Technology*, Vol. 17, No. 6, pp. 1615–1621, 2006.

4. Bornert, M., F. Brémand, P. Doumalin, J.-C. Dupré, M. Fazzini, M. Grédiac, F. Hild, S. Mistou, J. Molimard, J.-J. Orteu, L. Robert, Y. Surrel, P. Vacher and B. Wattrisse, "Assessment of Digital Image Correlation Measurement Errors: Methodology and Results", *Experimental Mechanics*, Vol. 49, No. 3, pp. 353–370, 2009.

5. Bornert, M., P. Doumalin, J.-C. Dupré, C. Poilâne, L. Robert, E. Toussaint and B. Wattrisse, "Assessment of Digital Image Correlation Measurement Accuracy in the Ultimate Error Regime: Improved Models of Systematic and Random Errors", *Experimental Mechanics*, Vol. 58, No. 1, pp. 33–48, 2018.

6. Fienup, J. R., "Invariant error metrics for image reconstruction", *Applied Optics*, Vol. 36, No. 32, p. 8352, 1997.

7. Lu, H. and P. D. Cary, "Deformation measurements by digital image correlation: Implementation of a second-order displacement gradient", *Experimental Mechanics*, Vol. 40, No. 4, pp. 393–400, 2000.

8. Schreier, H. W., "Systematic errors in digital image correlation caused by intensity interpolation", *Optical Engineering*, Vol. 39, No. 11, p. 2915, 2000.

9. Sutton, M., J. Yan, V. Tiwari, H. Schreier and J. Orteu, "The effect of out-of-plane motion on 2D and 3D digital image correlation measurements", *Optics and Lasers in Engineering*, Vol. 46, No. 10, pp. 746–757, 2008.

10. Lecompte, D., A. Smits, S. Bossuyt, H. Sol, J. Vantomme, D. Van Hemelrijck and A. Habraken, "Quality assessment of speckle patterns for digital image correlation", *Optics and Lasers in Engineering*, Vol. 44, No. 11, pp. 1132–1145, 2006.

11. Yaofeng, S. and J. H. Pang, "Study of optimal subset size in digital image correlation of speckle pattern images", *Optics and Lasers in Engineering*, Vol. 45, No. 9, pp. 967–974, 2007.

12. Pan, B., H. Xie, Z. Wang, K. Qian and Z. Wang, "Study on subset size selection in digital image correlation for speckle patterns", *Optics Express*, Vol. 16, No. 10, p. 7037, 2008.

13. Pan, B., Z. Lu and H. Xie, "Mean intensity gradient: An effective global parameter for quality assessment of the speckle patterns used in digital image correlation", *Optics and Lasers in Engineering*, Vol. 48, No. 4, pp. 469–477, 2010.

14. Hua, T., H. Xie, S. Wang, Z. Hu, P. Chen and Q. Zhang, "Evaluation of the quality of a speckle pattern in the digital image correlation method by mean subset fluctuation", *Optics & Laser Technology*, Vol. 43, No. 1, pp. 9–13, 2011.

15. Sutton, M. A., S. R. McNeill, J. D. Helm and Y. J. Chao, "Advances in Two-Dimensional and Three-Dimensional Computer Vision", P. K. Rastogi (Editor), *Photomechanics*, pp. 323–372, Springer Berlin Heidelberg, Berlin, Heidelberg, 2000.

16. Pan, B., "Bias error reduction of digital image correlation using Gaussian pre-

filtering", *Optics and Lasers in Engineering*, Vol. 51, No. 10, pp. 1161–1167, 2013.

17. Grédiac, M., B. Blaysat and F. Sur, "A Robust-to-Noise Deconvolution Algorithm to Enhance Displacement and Strain Maps Obtained with Local DIC and LSA", *Experimental Mechanics*, Vol. 59, No. 2, pp. 219–243, 2019.

18. Reu, P., "Using Anti-aliasing Camera Filters for DIC: Does It Make a Difference?", L. Lamberti, M.-T. Lin, C. Furlong and C. Sciammarella (Editors), *Advancement of Optical Methods in Experimental Mechanics, Volume 3*, pp. 89–92, Springer International Publishing, Cham, 2018.

19. Schreier, H. W. and M. A. Sutton, "Systematic errors in digital image correlation due to undermatched subset shape functions", *Experimental Mechanics*, Vol. 42, No. 3, pp. 303–310, 2002.

20. Yu, L. and B. Pan, "The errors in digital image correlation due to overmatched shape functions", *Measurement Science and Technology*, Vol. 26, No. 4, p. 045202, 2015.

21. Psarakis, E. and G. Evangelidis, "An enhanced correlation-based method for stereo correspondence with subpixel accuracy", *Tenth IEEE International Conference on Computer Vision (ICCV'05) Volume 1*, pp. 907–912 Vol. 1, IEEE, Beijing, China, 2005.

22. Tong, W., "An Evaluation of Digital Image Correlation Criteria for Strain Mapping Applications", *Strain*, Vol. 41, No. 4, pp. 167–175, 2005.

23. Bruck, H. A., S. R. McNeill, M. A. Sutton and W. H. Peters, "Digital image correlation using Newton-Raphson method of partial differential correction", *Experimental Mechanics*, Vol. 29, No. 3, pp. 261–267, 1989.

24. Chapra, S. C. and R. P. Canale, *Numerical methods for engineers*, McGraw-Hill Education, New York, NY, seventh edition edn., 2015.

25. Vendroux, G. and W. G. Knauss, "Submicron deformation field measurements: Part 2. Improved digital image correlation", *Experimental Mechanics*, Vol. 38, No. 2, pp. 86–92, 1998.

26. Pan, B., K. Li and W. Tong, "Fast, Robust and Accurate Digital Image Correlation Calculation Without Redundant Computations", *Experimental Mechanics*, Vol. 53, No. 7, pp. 1277–1289, 2013.

27. Pan, B. and K. Li, "A fast digital image correlation method for deformation measurement", *Optics and Lasers in Engineering*, Vol. 49, No. 7, pp. 841–847, 2011.

28. Pan, B., "An Evaluation of Convergence Criteria for Digital Image Correlation Using Inverse Compositional Gauss-Newton Algorithm: An Evaluation of Convergence Criteria for DIC", *Strain*, Vol. 50, No. 1, pp. 48–56, 2014.

29. Heath, M. T. and Society for Industrial and Applied Mathematics, *Scientific computing: an introductory survey*, 2018, oCLC: 1060647931.

30. Pan, B., W. Dafang and X. Yong, "Incremental calculation for large deformation measurement using reliability-guided digital image correlation", *Optics and Lasers in Engineering*, Vol. 50, No. 4, pp. 586–592, 2012.

31. Knauss, W. G., I. Chasiotis and Y. Huang, "Mechanical measurements at the micron and nanometer scales", *Mechanics of Materials*, Vol. 35, No. 3-6, pp. 217–231, 2003.

32. Huang, J., X. Pan, X. Peng, Y. Yuan, C. Xiong, J. Fang and F. Yuan, "Digital Image Correlation with Self-Adaptive Gaussian Windows", *Experimental Mechanics*, Vol. 53, No. 3, pp. 505–512, 2013.

33. Tu, P., "Digital image correlation with self-adaptive scheme for interpolation bias reduction", *Measurement Science and Technology*, Vol. 28, No. 7, p. 075008, 2017.

34. Yuan, Y., J. Huang, X. Peng, C. Xiong, J. Fang and F. Yuan, "Accurate displacement measurement via a self-adaptive digital image correlation method based on a weighted ZNSSD criterion", *Optics and Lasers in Engineering*, Vol. 52, pp. 75–85, 2014.

35. Cofaru, C., W. Philips and W. Van Paepegem, "A novel speckle pattern—Adaptive digital image correlation approach with robust strain calculation", *Optics and Lasers in Engineering*, Vol. 50, No. 2, pp. 187–198, 2012.

36. Cinar, A., S. Barhli, D. Hollis, M. Flansbjer, R. Tomlinson, T. Marrow and M. Mostafavi, "An autonomous surface discontinuity detection and quantification method by digital image correlation and phase congruency", *Optics and Lasers in Engineering*, Vol. 96, pp. 94–106, 2017.

37. Turner, D. Z., "Peridynamics-Based Digital Image Correlation Algorithm Suitable for Cracks and Other Discontinuities", *Journal of Engineering Mechanics*, Vol. 141, No. 2, p. 04014115, 2015.

38. Wang, B. and B. Pan, "Subset-based local vs. finite element-based global digital image correlation: A comparison study", *Theoretical and Applied Mechanics Letters*, Vol. 6, No. 5, pp. 200–208, 2016.

39. Ma, S., Z. Zhao and X. Wang, "Mesh-based digital image correlation method using higher order isoparametric elements", *The Journal of Strain Analysis for Engineering Design*, Vol. 47, No. 3, pp. 163–175, 2012.

40. Aydıner, C. C. and M. A. Telemez, "Multiscale deformation heterogeneity in twinning magnesium investigated with in situ image correlation", *International Journal of Plasticity*, Vol. 56, pp. 203–218, 2014.

41. Langtangen, H. P. (Editor), *Python Scripting for Computational Science*, Vol. 3 of *Texts in Computational Science and Engineering*, Springer Berlin Heidelberg, Berlin, Heidelberg, 2008.

42. Özdür, N. A., *Robust DIC*, 2019, `https://bitbucket.org/ccateam/robustdic/`, accessed at June 2019.

43. Gonzalez, R. C. and R. E. Woods, *Digital image processing*, Pearson, New York, NY, 2018.

44. Mazzoleni, P., F. Matta, E. Zappa, M. A. Sutton and A. Cigada, "Gaussian pre-filtering for uncertainty minimization in digital image correlation using numerically-designed speckle patterns", *Optics and Lasers in Engineering*, Vol. 66, pp. 19–33, 2015.

45. van der Walt, S., J. L. Schönberger, J. Nunez-Iglesias, F. Boulogne, J. D. Warner, N. Yager, E. Gouillart and T. Yu, "scikit-image: image processing in Python", *PeerJ*, Vol. 2, p. e453, 2014.

46. Xavier, J., "Measuring displacement fields by cross-correlation and a differential technique: experimental validation", *Optical Engineering*, Vol. 51, No. 4, p. 043602, 2012.

47. Bradski, G., "The OpenCV Library", *Dr. Dobb's Journal of Software Tools*, 2000.

48. Fischler, M. A. and R. C. Bolles, "Random sample consensus: a paradigm for model fitting with applications to image analysis and automated cartography", *Communications of the ACM*, Vol. 24, No. 6, pp. 381–395, 1981.

49. Jones, E., T. Oliphant, P. Peterson *et al.*, *SciPy: Open source scientific tools for Python*, 2001, `http://www.scipy.org/`, accessed at June 2019.

50. Fazzini, M., S. Mistou, O. Dalverny and L. Robert, "Study of image characteristics on digital image correlation error assessment", *Optics and Lasers in Engineering*, Vol. 48, No. 3, pp. 335–339, 2010.

51. Shannon, C. E., "A Mathematical Theory of Communication", *Bell System Tech-*

nical Journal, Vol. 27, No. 3, pp. 379–423, 1948.

52. Hartigan, J. A. and M. A. Wong, "Algorithm AS 136: A K-Means Clustering Algorithm", *Applied Statistics*, Vol. 28, No. 1, p. 100, 1979.

53. Pedregosa, F., G. Varoquaux, A. Gramfort, V. Michel, B. Thirion, O. Grisel, M. Blondel, A. Müller, J. Nothman, G. Louppe, P. Prettenhofer, R. Weiss, V. Dubourg, J. Vanderplas, A. Passos, D. Cournapeau, M. Brucher, M. Perrot and d. Duchesnay, "Scikit-learn: Machine Learning in Python", *arXiv:1201.0490 [cs]*, 2012, arXiv: 1201.0490.

54. Chen, Z. and S. Daly, "Deformation twin identification in magnesium through clustering and computer vision", *Materials Science and Engineering: A*, Vol. 736, pp. 61–75, 2018.

55. Rousseeuw, P. J., "Silhouettes: A graphical aid to the interpretation and validation of cluster analysis", *Journal of Computational and Applied Mathematics*, Vol. 20, pp. 53–65, 1987.

56. Powell, M. J. D., "An efficient method for finding the minimum of a function of several variables without calculating derivatives", *The Computer Journal*, Vol. 7, No. 2, pp. 155–162, 1964.

57. Wang, Z., A. Bovik, H. Sheikh and E. Simoncelli, "Image Quality Assessment: From Error Visibility to Structural Similarity", *IEEE Transactions on Image Processing*, Vol. 13, No. 4, pp. 600–612, 2004.

58. Ushizima, D., T. Perciano and D. Parkinson, "Fast detection of material deformation through structural dissimilarity", *2015 IEEE International Conference on Big Data (Big Data)*, pp. 2775–2781, IEEE, Santa Clara, CA, USA, 2015.

59. Lev, J., "The Point Biserial Coefficient of Correlation", *The Annals of Mathematical Statistics*, Vol. 20, No. 1, pp. 125–126, 1949.